Morphology of the forced oscillatory flow past a finite-span wing at low Reynolds number

By K. PARKER[1], K. D. von ELLENRIEDER[2] and J. SORIA[1]

[1]Laboratory for Turbulence Research in Aerospace & Combustion, Mechanical Engineering,
Monash University, Clayton Campus, Victoria, 3800 Australia
[2]Department of Ocean Engineering, Florida Atlantic University, Dania Beach,
FL 33004-3023, USA

A study of the morphology of the vortical skeleton behind a flapping NACA0030 wing with a finite aspect ratio of 3, is undertaken. The motivation for this work originates with the proposal that thrust can be efficiently produced by flapping aerofoils. The test condition corresponds to a Strouhal number of 0.35, Reynolds number, based on aerofoil chord, of 600 and an amplitude of flapping, equal to the chord length of the wing. This test condition corresponds to the optimal thrust-producing case in infinite-span flapping wings. This study investigates the effect of wing three-dimensionality on the structure of the wake-flow. This is accomplished here, by quantitatively describing the spatio-temporal variations in the velocity, vorticity and Reynolds stresses for the finite-span-wing case.

Preliminary flow visualizations suggest that the presence of wingtip vortices for the three-dimensional-wing case, create a different vortical structure to the two-dimensional-wing case. In the case of a two-dimensional-wing, the flow is characterized by the interaction of leading- and trailing-edge vorticity, resulting in the formation of a clear reverse Kármán vortex street at the selected test condition. In the case of a three-dimensional-wing, the flow exhibits a high degree of complexity and three-dimensionality, particularly in the midspan region. Using phase-averaged particle image velocimetry measurements of the forced oscillatory flow, a quantitative analysis in the plane of symmetry of the flapping aerofoil was undertaken. Using a triple decomposition of the measured velocities, the morphological characteristics of the spanwise vorticity is found to be phase correlated with the aerofoil kinematics. Reynolds stresses in the direction of oscillation are the dominant dissipative mechanism. The mean velocity profiles resemble a *jet*, indicative of thrust production. Pairs of strong counter-rotating vortices from the leading- and trailing-edge of the aerofoil are shed into the flow at each half-cycle. The large-scale structure of the flow is characterized by constructive merging of spanwise vorticity. The midspan region is populated by cross-sections of interconnected vortex rings.

1. Introduction

1.1. *Biomimesis*

As the priorities of ecology and economy change, so does the need for scientists to find alternative and more efficient means of transport. To this end, scientists have looked to nature for alternative and unconventional methods of propulsion.

The ability of some animal species to propel themselves efficiently, has created further interest in understanding the locomotive aspects of their propulsion. Cetaceans,

birds and insects share a common mechanism of propulsion, namely, the flapping motion of their lift-generating wings. DeLaurier & Harris (1982) explains that the optimal propulsive efficiency with which some species, such as sharks, are able to propel themselves, compared to their apparent lack of hydrodynamic efficiency has led to Gray's paradox. Nonetheless, the improvements in measurement techniques are providing opportunities to further understand, and use naturally occurring technology.

We investigate a particular adaptation of biomimesis. Biomimesis is the use of naturally occurring technology in modern engineering applications. Of specific interest, is the production of thrust by flapping wings. This propulsive technique is efficiently employed by species of cetaceans, insects and bird. According to Triantafyllou *et al.* (2000), the combination of heave and pitch oscillations in carrangiform motion, which is employed by some cetaceous creatures is highly evolved and efficient. Observations of this kind coupled with the potential for application of this technology has resulted in many hydrodynamic studies and has also enhanced our understanding of the many aspects of animal locomotion (Drucker & Lauder 1999). Nonetheless, our ability to apply this technology efficiently is still at its infancy.

1.2. *Flapping wings*

Knoller (1909) and Betz (1912) were among the first to investigate experimentally the effect of an aerofoil pitch oscillation on the free-stream flow. These studies determined that the oscillation induced an angle of attack such that the lift vector tilted in the free-stream direction, contributing to the thrust force.

Freymuth (1988) and Koochesfahani (1989) studied quantitatively and qualitatively, the flow patterns behind infinite-span aerofoils performing pure pitch oscillations. Koochesfahani (1989) presented some flow visualizations of a reverse Kármán vortex street under certain conditions defined by the dimensionless Strouhal number. In the Strouhal range of $0 \leqslant St \leqslant 5$, the reverse Kármán vortex street suggested velocity addition to the flow, producing thrust. Simultaneously, numerical methods have been used to determine the accuracy of various theoretical flow models in predicting the properties of the flow, including the thrust. Katz & Weihz (1978) used a panel method to study the effects of various flapping motions on thrust. Garrick (1936) applied an inviscid, unsteady, thin aerofoil theory to a two-dimensional aerofoil and found that this was unsuitable for simulating the flow mechanics behind pitching aerofoils. Another study by Tuncer, Walz & Platzer (1998) identified parameters that influenced dynamic stall. Their study, like most others, focuses primarily on parametrically measuring the unsteady effects of oscillating aerofoils including aero-elastic flutter, rather than investigating the flow physics that cause them.

Investigations into heaving aerofoil flows have also provided valuable information on the flow physics related to flapping wings. Jones, Dohring & Platzer (1996) and Platzer (2001) provided a comprehensive experimental and numerical analysis, on the thrust-producing ability of infinite-span pure heaving aerofoils. The reduced frequency, $k = \omega c / 2 U_\infty$, was used as the principal parameter to predict thrust production in heaving aerofoils. Jones *et al.* (1996) parametrically investigated the effect of other motion parameters and found that heave amplitude and oscillation frequency were important for the production of efficient thrust.

It is assumed that creatures that flap their wings to propel themselves, do so with optimal efficiency. The motion can be simply characterized by combining heave and pitch oscillations. Anderson *et al.* (1998) and Triantafyllou *et al.* (2000) conducted extensive parametric particle image velocimetry (PIV) measurements on the factors

that influence the thrust-producibility of flapping wings. They found that the dimensionless Strouhal number, *St*, can be principally used to describe the condition for thrust production. This parameter, defined in (1.1) is also appropriate to define a characteristic wake pattern. The term *wake* is used here to describe the location of the measurement rather than a drag indicative velocity scenario.

$$St = \frac{fA}{U_\infty}, \tag{1.1}$$

where f is equal to the frequency of oscillation (heave frequency is equal to pitch frequency), A represents the maximum excursion of the aerofoil trailing-edge ($=$ double-amplitude of oscillation, $=c$) and U_∞ represents the free-stream velocity. According to Anderson (1996), the phase relationship between heave and pitch oscillations, as well as the maximum angle of attack of the aerofoil in pitch oscillations will also influence the ability of an oscillating aerofoil to produce thrust optimally. Studies such as this have significantly enhanced our understanding of the mechanics behind flapping-foil thrust production. Yet thrust production is not the only result of flapping wings.

On the other hand, a study of active vorticity control through the use of a flapping aerofoil upstream of a stationary cylinder or aerofoil, resulted in the establishment of the Katzmayr effect (Katzmayr 1922). The flapping aerofoil can exert a degree of control on the boundary layer and flow characteristics of the downstream aerofoil or cylinder through phase locking of the vorticity-shedding process with the motion of the upstream forcing of the oscillating aerofoil. The basis for enhancing performance through unsteady flow control is the formation of large-scale vortices through body motion, the sensing and manipulation of the vortices as they move down the body, and the efficient repositioning through trailing-edge motions. In this case, the manipulation of the wake or boundary layer through adaptive repositioning is a consequence of the neighbouring flapping motion as well.

Cheng & Murillo (1984) first raised the concern that many of the predictions of thrust forces and thrust efficiencies were overestimated. They were also concerned that any representations of the wake structure were erroneous. In both cases, these concerns were due to the absence of wingtip effects in the investigations. For example, the work by Anderson *et al.* (1998) is one of the most comprehensive studies of flapping aerofoils. It investigates the interaction between the flow physics, wake structure and thrust producibility. However, the study is based on two-dimensional-aerofoils. While it does provide a baseline for comparison with the three-dimensional-aerofoil studies undertaken here, it does not account for the interaction of bound wingtip vorticity with leading- and trailing-edge vortices. In nature, as in engineering applications, bodies have finite aspect ratios and are three-dimensional in nature. While increasing efforts are being made to determine the effects of wing three-dimensionality on thrust and wake characteristics, using numerical techniques (Jones *et al.* 2002), generally, there are few experimental data.

Preliminary experiments by von Ellenrieder, Parker & Soria (2003) suggest that wingtip vortices on a three-dimensional wing would reduce the efficiency values that have been reported. They show using flow visualizations, that the coupled interaction between wingtip vortices and vorticity shed from the leading- and trailing-edge of a flapping wing, creates a flow topology significantly different to the conventional reverse Kármán vortex street. From Parker *et al.* (2002*a*), the typical flow pattern behind a two-dimensional-aerofoil is illustrated in figure 1. On the other hand, based on the results of von Ellenrieder *et al.* (2003), a model of the flow skeleton behind a finite-span
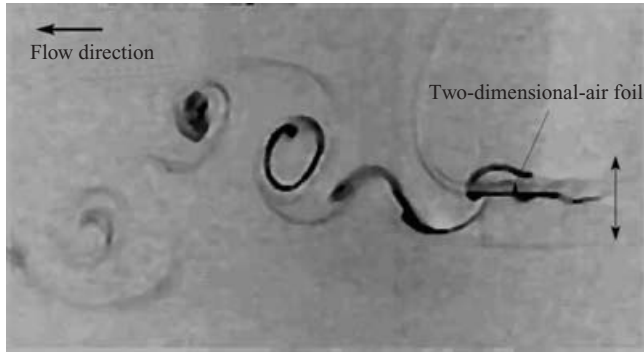
FIGURE 1. Dye flow visualization of the flow behind a wing with NACA0030 profile and aspect ratio $= 3$. For the condition shown, $St = 0.35$, $\theta_0 = 10°$ and $\psi = 90°$.
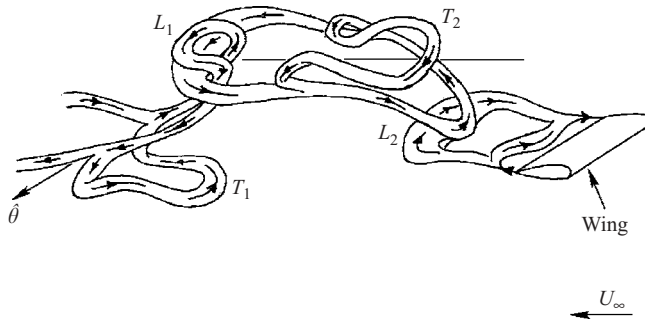

FIGURE 2. Proposed three-dimensional structure of the vortex skeleton behind a wing with NACA0030 profile and aspect ratio $= 3$. For the condition shown, $St = 0.35$, $\theta_0 = 10°$ and $\psi = 90°$. Flow is from right to left.

aerofoil is presented in figure 2. It can be seen that the flow topology is inherently more complex for the three-dimensional case. According to Bishop & Hassan (1963), there is a direct relationship between flow topology, body kinematics and the forces imparted to the flow. Therefore, the observed variation in the flow topology is expected to significantly modify the dynamics of interaction between vortical structures that constitute the flow, and ultimately also the thrust producibility. Hence, the need for further work.

Moreover, parametric visualization experiments by Parker *et al.* (2003, 2002*b*) have identified the separate effects of oscillation frequency, amplitude and phase angle between heaving and pitching oscillations, on the structure of the flow behind a finite-span aerofoil with aspect ratio 3. Overall, the results corroborate many features of the model in figure 2. Numerical studies by Guglielmini & Blondeaux (2004) and Triantafyllou, Techert & Hover (2004), have predicted similar flow patterns for the same flow conditions. Buchholz & Smits (2005) observed a wake dividing into two chains of vortical structures with an appearance very different from that observed by von Ellenrieder *et al.* (2003). They also mentioned that this was observed by Blondeaux *et al.* (2005*a*). However, in the case of Buchholz & Smits (2005), the flow behind a low-aspect-ratio flat plate, which undergoes a purely pitching motion was investigated. The results of their work cannot be directly compared to previous pitching/heaving aerofoil studies as the geometry and flow conditions of their experiment are different. The pitching plate oscillates about its leading-edge and behaves more like a

trailing-edge flap as it is mounted in the wake of a stationary aerofoil. Furthermore, on closer investigation of the work of Blondeaux *et al.* (2005*a*), no two chains of vortical structures were originally reported. The comments of Buchholz & Smits (2005) are therefore potentially misleading.

The aim of the current paper is not to reproduce the three-dimensional structure proposed in von Ellenrieder *et al.* (2003), but to present quantitative measurements performed at a specific test condition. The methodology adopted has also been tested in Parker *et al.* (2005). We focus on the quantitative description of the evolution of spanwise vorticity in the plane of symmetry. Based on the flow visualizations of von Ellenrieder *et al.* (2003) this was a logical choice. The limitations associated with qualitative flow visualizations of unsteady flow structures are discussed by Hama (1962). In order to test the interpretations from the qualitative measurements, as well as provide quantitative data for comparison with numerical results, measurements of the flow behind a finite-span flapping wing are required. For this purpose, Non-intrusive planar PIV measurements are conducted in the plane of symmetry of a wing with a finite span. The parameters selected for experimentation allow comparison with previous studies by Anderson *et al.* (1998) and von Ellenrieder *et al.* (2003).

The test condition corresponds to the optimal thrust-producing case for an infinite-span aerofoil, as measured by Anderson *et al.* (1998). Parker *et al.* (2002*a*,*b*, 2003) parametrically investigated the effect of this test condition and others, on a finite-span aerofoil and found significant qualitative differences for all cases. Moreover, Parker *et al.* (2004, 2005) found that the present test condition produced some unique features in the resulting wake-flow, particularly along the wing midspan, where measurements are now conducted. Using a method similar to Hussain & Reynolds (1970), the measured oscillatory flow is decomposed into coherent and incoherent components. This allows the processes responsible for Reynolds stresses, to be decomposed into coherent and incoherent parts. The aim of this study is to quantitatively describe some evolutionary characteristics of this highly complex flow.

2. Experimental technique and apparatus

2.1. *Apparatus*

The experiments were conducted in a water tunnel at the Laboratory for Turbulence Research for Aerospace & Combustion (LTRAC). The tunnel has a 5 m long test section, with 500 mm × 500 mm cross-section. The recirculating water tunnel is capable of delivering speeds up to $1 \, \mathrm{m \, s^{-1}}$. The experimental set-up is shown in figure 3.

The turbulence intensity in the core region of the test section is less than 0.35 %. The turbulence intensity here, is calculated from the fluctuating components of the in-plane velocities, u and v. The variation of the turbulence intensity across the tunnel width is shown in figure 4(*a*). The mean velocity profile across the width of the test section is shown in figure 4(*b*). The mean profile is measured using PIV and 1000 instantaneous image pairs. From figure 4(*b*), the mean profile in the core region of the test section is stable, with minimal variation. Experimental measurements are acquired in this region. The profile is similar to a wall-bounded flow in a channel (Pope 2000). The mean tunnel centreline velocity is $30 \, \mathrm{mm \, s^{-1}}$, corresponding to a Reynolds number, based on the tunnel width, of 15 000, at 23 °C.

A NACA0030 aerofoil, with chord, $c = 20$ mm and aspect ratio, $AR = b/c = 3$ is suspended vertically above the test section. The aerofoil assembly can be seen in figure 3. The aerofoil performs angular (pitch) and lateral (heave) oscillations in the y-direction, using stepper motors. The aerofoil heaves in the y-direction and pitch
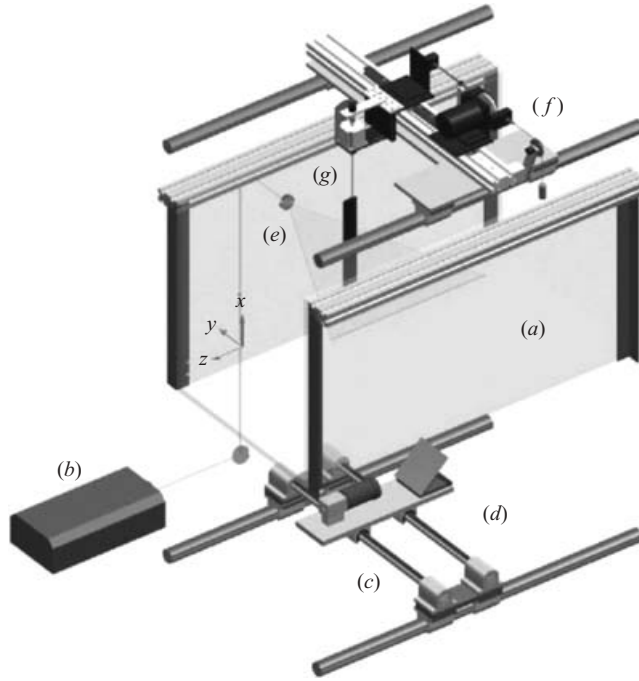
FIGURE 3. Schematic of the experimental apparatus: (*a*) test section, (*b*) laser, (*c*) CCD camera, (*d*) 45° mirror, (*e*) light sheet, (*f*) heaving stepper motor with Scotch yoke, (*g*) pitch stepper motor.
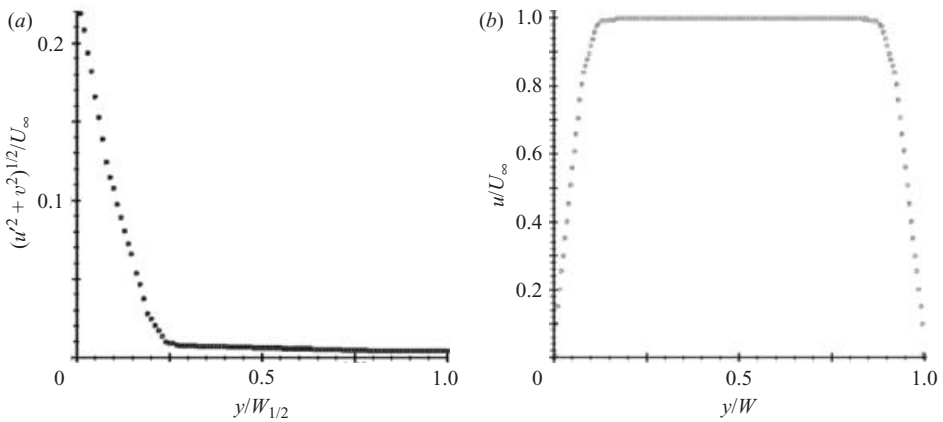

FIGURE 4. (*a*) Non-dimensional turbulence intensity in the test section at $30\,\mathrm{mm\,s^{-1}}$. (*b*) Mean streamwise non-dimensional velocity profile across the test section at $30\,\mathrm{mm\,s^{-1}}$. U_∞ is the free-stream velocity and $W_{1/2}$ is the test section half-width.

oscillates about the quarter-chord, $c/4$ location. The aerofoil is vertically supported at the quarter-chord position which corresponds approximately to the aerodynamic centre for this symmetrical aerofoil. The heave-stepper motor performs the oscillations by virtue of a Scotch yoke. The Scotch yoke drives a platform mounted on a linear bearing. A second stepper motor is mounted on this platform and drives the aerofoil directly. The stepper motor motions can be accurately controlled using an in-house
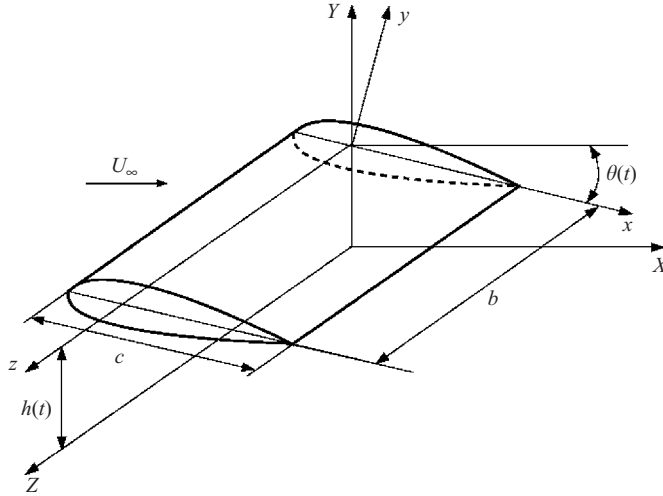
FIGURE 5. Schematic of the aerofoil motion in the reference frame (X, Y, Z) of the free-stream velocity, U_∞, and the reference frame (x, y, z) of the aerofoil.

developed motion control program, which interfaces with a Motion Architect AT6400 multi-axis motor controller.

The controller controls each Rorze stepper motor driver. The control program allows different motion parameters, such as frequency of oscillation, f, maximum pitch oscillation amplitude, θ_0 and phase angle between heaving and pitching oscillations, ψ, to be independently varied. Thereby, allowing for various motion profiles to be reproduced by the aerofoil. The oscillating mechanism and aerofoil was appropriately modified to avoid undesirable excitation of the resonant frequency by the forcing frequency of oscillation. This could create or amplify any disturbances in the flow and modify the true structure under investigation. The natural frequency of the system is 17.13 Hz while the forcing frequency of the aerofoil is 0.5 Hz.

The entire oscillating mechanism is mounted on a railing system above the test section, allowing the aerofoil set-up to be moved to different free-stream locations in the test section. Once the CCD camera and laser sheet are appropriately positioned to image the desired area in the measured plane, only the aerofoil need be adjusted, relative to the fixed measurement plane, to measure other spanwise locations. This set-up is conducive to repeatable measurements.

The heave, $h(t)$, and pitch, $\theta(t)$, oscillations have a sinusoidal profile according to,

$$h(t) = h_0 \cos(\omega t), \tag{2.1}$$
$$\theta(t) = \theta_0 \cos(\omega t + \psi), \tag{2.2}$$

where, $h_0 = c/2$ and $\omega = 2\pi f$ (equal for heave and pitch oscillations). h_0 and θ_0 are the maximum excursions of the trailing-edge of the aerofoil. Figure 5 shows the aerofoil motion parameters in a Cartesian reference frame. The oscillation profiles in (2.1) and (2.2), are based on past studies on the effect of various motion profiles, on thrust producibility and vortex pattern formation. Koochesfahani (1989) used flow visualizations and found that a sinusoidal variation produced the clearest reverse Kármán vortex street associated with thrust production with maximum efficiency. Anderson (1996) found similar results, based on two-dimensional aerofoil measurements, later corroborated by Hover, Haugsdal & Triantafyllou (2003). In the

Parameter	Quantity
c	20 mm
AR	3
St	0.35
Re_c	600
θ_0	5°
h_0	0.5c
ψ	90°
ϵ_θ	0.05°
ϵ_h	0.003125c
ϵ_{z_s}	0.00127c

TABLE 1. Experimental set-up parameters.

flow visualizations of von Ellenrieder *et al.* (2003), the motion profile in (2.1) and (2.2) produced the flow structure shown in figure 2.

It is important for the aerofoil to follow the planned trajectory accurately, without any deviations caused by jitter. If the aerofoil is allowed to stray from the design path, the resulting flow would not be representative of the input forcing motion. In order to ensure accurate and repeatable motion of the aerofoil, wheel-potentiometers were modified to fit in-line with the drive axes of the stepper motors. Thus, a continuous measure of the output motion of the aerofoil is available. Optical sensors are placed at $h = 0$, $h = h_0$ and $\theta = \theta_0$ positions. Whilst providing a means of checking the frequency, f and phase ψ, as measured by the potentiometers, the sensors provide a 5 V trigger signal used for PIV image acquisition. To check for jitter, instantaneous images are acquired at a fixed aerofoil pitch and heave location. Groups of 4, 8, 16 and 64 images were averaged and the jitter in the resulting image was measured in pixels. The measured error in the pitch and heave oscillation is ϵ_θ and ϵ_h, respectively, is given in table 1.

2.2. *PIV image acquisition*

In order to quantitatively analyse the flow, digital particle image velocimetry is used. PIV measurements are conducted in the near-wake region of the aerofoil. The wing is fully submerged and measurements are conducted in the plane of symmetry (midspan) of the wing. A region $4c$ in the transverse direction (y) by $3c$ in the streamwise direction (x) is captured. Based on the flow visualizations of von Ellenrieder *et al.* (2003), this area is large enough to capture the large-scale structure of the flow resulting from one complete flapping oscillation of the aerofoil.

Prior to the PIV acquisition, the flow was uniformly seeded with Potters hollow glass beads, nominally 11 μm in diameter and with specific gravity of 1.1. The particles are premixed in a beaker, into a paste, using a surfactant and water from the test section. The mixture is placed on a magnetic stirrer and the larger particles, that dissociate from the mixture, are separated and discarded. In order to further facilitate mixing prior to measurements in the test section, the tunnel speed is rapidly increased for several minutes after the particles have been added. Thereafter, the tunnel flow speed is reduced to the test speed. The water is allowed to settle in approximately 10 min, before commencing experiments.

As illustrated in figure 3, a Pixelfly CCD camera, with array size 1280 pixels × 1024 pixels, is horizontally mounted below the test section and the flow above is observed through a large rectangular mirror mounted at 45° to the line of sight. The camera is fitted with a 105 mm Micro Nikkor Nikon lens set at an aperture of $f2.8$. A
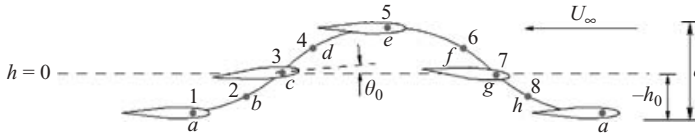
FIGURE 6. Heave and pitch motion profile for $\psi = 90°$. The solid line represents the path of the quarter-chord point, the letters $(a–h)$ indicate the labels in all visualization figures and the numbers indicate the aerofoil phase location according to table 3.

Parameter	Quantity
Magnification	0.06
dt	7.0 ms
Grid spacing	0.05c
IW$_0$	0.1c
IW$_1$	0.05c
MVR	0.25
MVC	1.3
d.o.f.	0.35c

TABLE 2. PIV image acquisition and analysis parameters.

reproduction ratio of 5 was used for all experiments. With these settings, the estimated aberration-free depth of field, d.o.f. $= 7$ mm and the diffraction limited particle image size was 7.7 μm. The camera arrangement is mounted on a railing system to allow easy x, y, z-translation to different locations in the flow. The camera captures the motion of the neutrally buoyant fluorescent particles that trace the motion of the flow. Using a dual-cavity New Wave Nd:YAG laser, two 532 nm laser beams are fired at 32 mJ each. Using the necessary collimating lens optics, a 3 mm thick horizontal light sheet is created in the midspan region of the aerofoil.

A real-time Linux program controls the entire PIV acquisition process. The image acquisition is synchronized with the laser firing. The acquisition process is triggered by the optical sensors tracking the motion of the aerofoil. Image pairs are acquired by the camera every 250 ms and the time between laser firing, d$t = 7$ ms. The size of the largest measured displacement is the maximum velocity ratio (MVR) and is at least 25 % of the sampling window used for the PIV analysis. The exposure time for the camera is 220 μm.

The set-up employed here permits image acquisitions that are phase locked with the motion of the aerofoil. Phase-averaged measurements are acquired at eight equally spaced locations along one heave cycle (figure 6). The period of one heave cycle is 2 s. At each phase, 500 instantaneous PIV image pairs are acquired.

The acquired double exposed image pairs are analyzed using a adaptive multi-grid cross-correlation algorithm (MCCDPIV) (Soria 1998). Based on the number of image pairs acquired and the measured standard deviation in the resolved velocities, a 1 % random error is estimated based on a statistical confidence of 99 %. The acquired images are analysed using the parameters given in table 2.

2.3. *Vorticity calculation*

The out-of-plane vorticity, ω_z, was calculated from the MCCDPIV velocity field measurements using a local least-squares fit procedure to the velocity field, followed

by analytic differentiation (Soria 1996) using the relationship

$$\omega_z = \partial v/\partial x - \partial u/\partial y. \tag{2.3}$$

A thirteen-point two-dimensional local fit to the data was used. The additional bias and random error introduced by this approximation into the vorticity value have been investigated (Fouras & Soria 1998). The accuracy of the ω_z field measurement depends primarily on the spatial sampling distance between each velocity data point and the accuracy of the resolved velocity vector field. The ratio of the biased vorticity error, ω_{bias}, to the exact value of the vorticity, ω_{exact}, shown in (2.4) can be derived using the methodology outlined in Fouras & Soria (1998) and can be used to estimate the biased vorticity error.

$$\frac{\omega_{bias}}{\omega_{exact}} = -0.7478\left(\frac{\Delta}{L}\right)^{1.96}. \tag{2.4}$$

This relationship shows that the bias error is related to the sampling separation between velocity measurements, where L can be thought of as being a characteristic length scale of the vorticity distribution and Δ is the distance between adjacent velocity measurements.

The ratio of random error in the MCCDPIV velocity measurement compared to ω_z is denoted by λ_0 and can be calculated using the relationship derived in Fouras & Soria (1998) shown in (2.5). This relation is specific to the thirteen-point fitting technique used to calculate the vorticity.

$$\lambda_0 = \sqrt{\frac{1}{5}}\left(\frac{L}{\Delta}\right). \tag{2.5}$$

For a vorticity distribution with a characteristic length scale of 16Δ, the bias error is estimated as -0.3% and the random error is estimated as $\pm 2.0\%$ at the 99% confidence level, whereas for a vorticity distribution with a characteristic length scale of 4Δ, the bias error is estimated as -3.9% and the random error is estimated as $\pm 1.0\%$ at the 99% confidence level.

3. Non-dimensionalization and scaling

The velocity and spatial coordinates are non-dimensionalized by the uniform convection velocity, U_∞ and the chord, c, respectively. The total extent of travel of the aerofoil trailing-edge is $1c$. Therefore, it is considered that the spatial extent of any wake structure will scale with this length in the near-body region where the measurements are conducted. The aerofoil is forced according to (2.1) and (2.2). The vorticity is non-dimensionalized by the maximum rate of pitch oscillation, $\dot{\theta}_0 = 0.274 \text{ rad s}^{-1}$.

The mean profile in the aerofoil wake will indicate a velocity deficit or addition scenario. For the mean profiles, the velocity is non-dimensionalized by the maximum centreline velocity, $U_m = (U_c - U_\infty)$, where U_c is the mean centreline velocity of the jet. The transverse location, y, is non-dimensionalized by the wake half-width similar to Tennekes & Lumley (1972).

In some cases, streamlines are used to highlight salient features in the flow. The streamlines are confined to the two-dimensional projection of the flow in (x, y)-space and are calculated from the $\langle u \rangle$ and $\langle v \rangle$ phase-averaged components of velocity, integrated along the free-stream direction. Streamlines are not Galilean invariant because they depend on the velocity of the observer. According to (Chong, Perry & Cantwell 1990), the complexity arises when integrated particle paths cross instantaneous
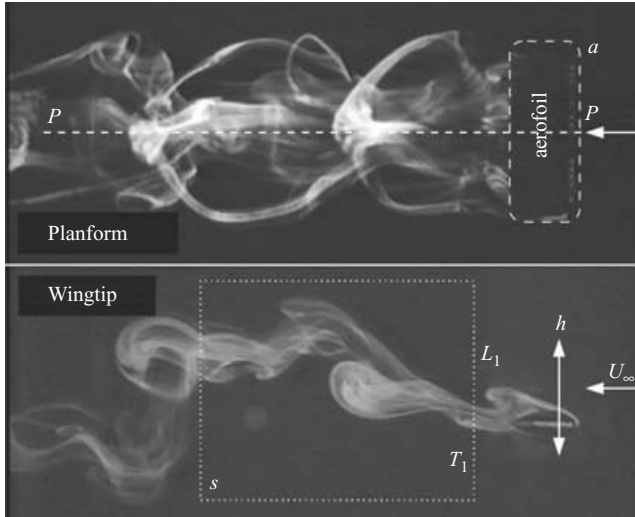
FIGURE 7. Dye flow visualization behind a three-dimensional flapping wing at $St = 0.35$, $Re = 600$. Flow is from right to left.

Phase ϕ	Figure label	ψ (deg.)	$h(t)$ (mm)	$\theta(t)$ (deg.)
1	a	180	-10	0
2	b	225	-7.07	$+3.5$
3	c	270	0	$+5.0$
4	d	315	$+7.07$	$+3.5$
5	e	0	$+10$	0
6	f	45	$+7.07$	-3.5
7	g	90	0	-5.0
8	h	135	-7.07	-3.5

TABLE 3. Heave and pitch locations for each phase at which PIV measurements are acquired.

streamlines, creating ambiguous structures. Nonetheless, their purpose here is to show the nature of the in-plane vector field flow in relation to closed orbits or spirals. The convection velocity, U_∞ is removed in order to obtain the frame of reference of an observer moving with the fluid.

4. Results

Figure 7 shows a typical flow visualization behind a finite-span flapping aerofoil from von Ellenrieder *et al.* (2003). From figure 7, it can be seen that the flow topology is highly complex, particularly along the plane of symmetry, marked by PP in the planform view of the aerofoil. Therefore, PIV measurements are conducted in this (x, y)-plane. The measurement domain is highlighted by region S in the wingtip view.

Table 3 gives the eight heave and pitch locations at which instantaneous images of the flow are acquired. Phase-averaged quantities are presented in figures 11 to 25 for each of the eight phases labelled alphabetically according to table 3. The figures for each of the phase locations have been labelled as indicated. The spatial variation in the (x, y)-plane, for each parameter, is represented by iso-contours in region S. The temporal variation is captured by the measurement at each phase. Together, the spatio-temporal variation in the flow is investigated.

Unless otherwise stated, flow is from left to right for all figures. The aerofoil heaves vertically, between $-h_0$ and $+h_0$, which in the figures presented, are indicated by $y/c = 1$ and $y/c = 2$, respectively. In all figures, a cartoon of the aerofoil, to scale, is inserted at the left-hand side of the image to provide a sense of the flow field relative to the orientation of the aerofoil. Using the resolved velocity vector fields, the vorticity and Reynolds stresses are calculated. Positive spanwise vorticity, $+\omega_x$, is counterclockwise (CCW) and out-of-the-page.

The test condition for the results correspond to $Re_c = 600$, $\theta_0 = 5°$, $\psi = 90°$ and $St = 0.35$. The free-stream velocity $U_\infty = 30 \, \text{mm s}^{-1}$. The maximum aerofoil heave oscillation velocity $\dot{h}_0 = 31.42 \, \text{mm s}^{-1}$. The aerofoil double amplitude of oscillation $2h_0 = c$. The aerofoil chord length, $c = 20 \, \text{mm}$.

5. Discussion of results

5.1. *Coherent and incoherent contributions to Reynolds stress*

The Reynolds number of the flow is low and it is expected that the Reynolds stress in the initial stages of development of the wake is predominantly due to the time-dependent nature of the reverse Kármán vortex street. While the Reynolds regime here does not produce a chaotic velocity and pressure field as would higher Reynolds numbers, the flow field is made up of some incoherent components from near-wake turbulence and instabilities in the separated shear layer. In the present case of forcing the aerofoil to oscillate at a prescribed frequency, the contribution of the incoherent random turbulence is expected to be negligible.

To examine more closely the different contributions to Reynolds stresses, the phase-averaging procedure suggested by Hussain & Reynolds (1970), Reynolds & Hussain (1972) and Cantwell & Coles (1983) is applied. In this case, the forced oscillation of the wing introduces a wave into the flow. Using the optical sensors in our experimental set-up, images of the flow are captured at discrete phase locations in the trajectory of the aerofoil. The flow can be decomposed into a mean and a hierarchy of coherent and incoherent motions of various length scales.

Hussain (1986) refers to the separation from instantaneous flow fields into coherent and incoherent parts, as eduction. Here, *phase average* denotes phase-aligned ensemble average. This is an average of successive structures at the same phase or age in the forced oscillation of the aerofoil. Thus, the phase average of structures of the same mode and parameter size is the coherent structure, and the departure of each instantaneous realization from the phase average denotes incoherent turbulence. By *mode* is meant the physical configuration (e.g. toroidal, helical, hairpin, etc.) of the structure. By *parameter size* is meant the shape, size, strength and convection velocity of a structure.

Through selective sampling, the organized wave motion can be separated from the background field of finite turbulent fluctuations. In the presence of such forced disturbances, in general, any fluctuating quantity $f(\boldsymbol{x}, t)$ can be triple decomposed. The flow variables $f(\boldsymbol{x}, t)$ are made up of three components: a global mean component $\overline{f}(\boldsymbol{x})$, a periodic mean component $\tilde{f}(\boldsymbol{x}, t)$ and a residual random component $f'(\boldsymbol{x}, t)$, such that

$$f(\boldsymbol{x}, t) = \overline{f}(\boldsymbol{x}) + \tilde{f}(\boldsymbol{x}, t) + f'(\boldsymbol{x}, t), \tag{5.1}$$

$$\tilde{f} = \langle f \rangle - \overline{f}. \tag{5.2}$$

The periodic mean represents the contribution of the organized wave (forcing function) to each instantaneous measurement. When added to the global mean
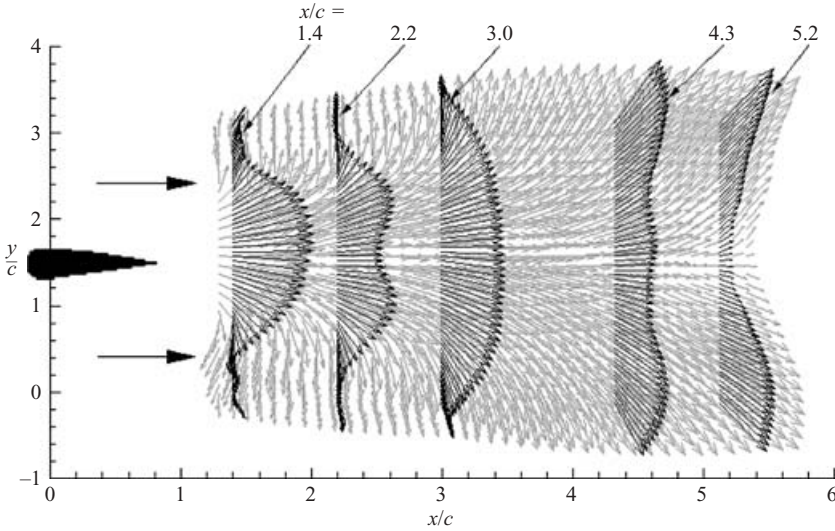
FIGURE 8. Mean velocity vector field measured behind a finite-span flapping aerofoil at $\theta_0 = 5°$, $\psi = 90°$, $St = 0.35$.

component the coherent component of the measured quantity is calculated. This quantity is defined also as the ensemble or phase-averaged component and is denoted by $\langle f \rangle$ in (5.2). In the present study, 500 instantaneous PIV images acquired at fixed locations of the wing motion-trajectory are used to calculate each phase average. Eight phases are used to track the evolution of the reverse Kármán vortex street, that is associated with thrust-producing flapping wings. On the other hand, an average of the coherent component, over all the different phases, will erase the phase information and result in the global mean component. The contribution of the random component or turbulence is represented by $f'(\boldsymbol{x}, t)$. The periodic and random components account for all fluctuations about the global mean.

Of particular interest is the contribution of the periodic mean $\tilde{f}$ and the global mean $\overline{f}$ components to the phase-acquired measurements, $\langle f \rangle$ of the forced wing oscillations. To this end, various periodic mean quantities are presented in the following sections and denoted by $\tilde{f}$, while the phase- or ensemble-averaged components are denoted by $\langle f \rangle$. The random incoherent turbulence, accounts for all other fluctuations, but is omitted in this study.

Using the triple decomposition approach, the Reynolds stress can be split into a coherent and an incoherent part. The random component in (5.1) accounts for all fluctuations, u'^2, v'^2 and $u'v'$. The coherent component of the Reynolds stress, taken over 500 image pairs per phase is denoted by $\langle u^2 \rangle$, $\langle v^2 \rangle$ and $\langle uv \rangle$. The periodic mean component is calculated from $\tilde{u}^2 = \langle u^2 \rangle - u'^2$, $\tilde{v}^2 = \langle v^2 \rangle - v'^2$ and $\tilde{u}\tilde{v} = \langle uv \rangle - u'v'$ in accordance with Reynolds & Hussain (1972).

5.2. Time-mean flow characteristics

The properties of the mean flow field can be determined by calculating $\overline{f}(\boldsymbol{x})$ in (5.1). The non-dimensionalized in-plane vector field, U/U_∞ and V/U_∞ is shown in figure 8 with mean profiles highlighted at $x/c = \{1.4, 2.2, 3.0, 4.3, 5.2\}$. These locations were randomly selected to look at the variation in the free-stream direction. The mean velocity, U_∞, has been subtracted from the mean streamwise velocity component so
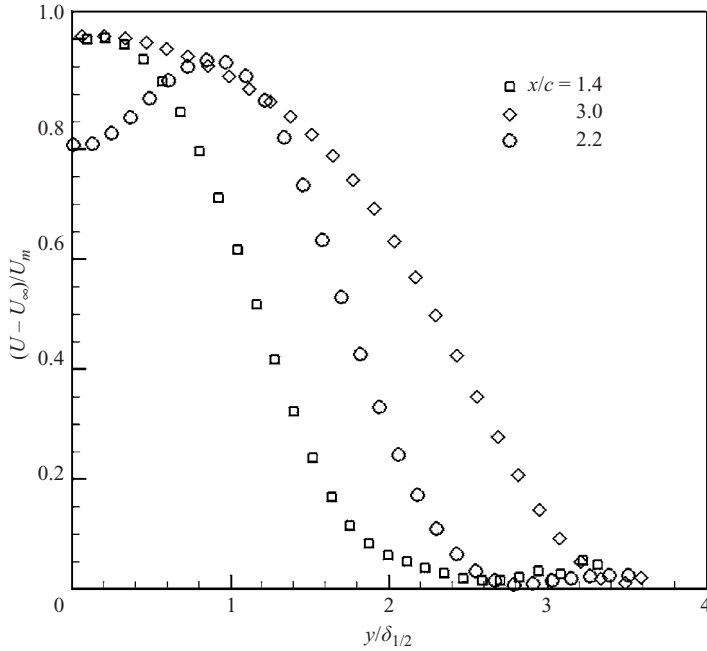
FIGURE 9. Average jet-velocity profiles as a function of jet half-width, $\delta_{1/2}$ at various downstream stations in the flow field behind a three-dimensional flapping foil.

that the vector field represents the velocity addition. Every second vector is shown and the vector size has been abnormally increased in order to make the profiles obvious.

In all x/c cases, the mean in-plane velocity profile in figure 8 has a jet-like profile in the axial direction. At $x/c = 1.4$, the profile exhibits some asymmetry about the mean heave axis at $y/c = 1.5$. In the case of $x/c = 2.2$, the profile is symmetrical about the mean heave-oscillation axis at $y/c = 1.5$. For a jet flow scenario, a uniform velocity profile similar to a round or plane jet was expected, as shown in Pope (2000). At $x/c = 2.2$, the mean axial velocity profile exhibits a double hump symmetric about the mean heave axis. The double hump is generally synonymous with swirling flows (Lozano, Kostas & Soria 1998). It is thought that the two large-scale counter-rotating vortical structures measured on either side of $h = 0$, in the phase measurements in figure 19 are responsible for the modification of the mean profile. Coupled with the interaction of the wingtip vortices, a swirl-like component could be introduced. However, the mean profile returns to a regular shape at $x/c = 3.0$, suggesting that if the vortical structures are responsible for this modification, they are spatially biased to the region $x/c = 2.2$.

To investigate the mean velocity profiles more closely, figure 9 shows the mean axial velocity minus the free-stream velocity, U_∞, non-dimensionalized by the maximum velocity addition along the centreline, U_m, against the jet half-width, $\delta_{1/2}$. The cases of $x/c = \{1.4, 2.2, 3.0\}$ are shown. Every second vector is shown. Since the measurement are close to the aerofoil, the jet has not had time to develop fully. Therefore, the profiles are not expected to be self-similar. According to Pope (2000), the development length in round jets is nominally from 30 jet diameters. The velocity addition in the wake region is indicative of net thrust production. Although 'wake' would normally define a region of velocity deficit, here it will be used to describe the region of the flow

behind the aerofoil which clearly shows jet behaviour. At $x/c = 1.4$ and 3.0, the profile has a conventional Gaussian distribution with jet half-width. This is most evident at locations with $x/c < 3$, where the wake width appears small enough to be captured in its entirety. Further downstream, the wake grows and the jet-like profile is not as obvious. At $x = 1.4c$, the wake width is roughly $2c$. The width here is measured from the first occurrence of the free-stream velocity on either end of the profile. Further downstream, at $x/c = 4.3$, a triple hump is just visible, but then the profile resembles more of a wake at $x/c = 5.2$. In general, the mean profile exhibits some differences from a conventional jet profile.

5.3. *Velocity and vorticity fields*

The spatio-temporal variation of the periodic mean in-plane velocity component, $(\tilde{U}\tilde{V})$, is presented in figures 11 to 18. The velocities are represented by streamlines. The streamlines overlap iso-contours of the spanwise vorticity. The corresponding vector field is shown in figure 19.

The coherent streamline patterns indicate the presence of two large recirculating structures occupying the bulk of the measured area. The counter-rotating structures have their focus on either side of the mean heave axis, but are spatially non-overlapping. The distribution and convection of the streamline patterns over one cycle indicates that the flow is strongly influenced by the disturbances introduced by the aerofoil motion. The shedding of spanwise vorticity into the flow appears to be phase locked with the motion of the aerofoil.

In one cycle, two distinct structures formed by the streamlines, are observable. The circulation of these structures are marked A and B in figure 13. The arrangement of these large-scale structures form a counter-rotating pair about the mean oscillation axis, $h = 0$. The dashed line in figure 13 indicates $h = 0$. The foci created by the streamlines overlap with the regions of intense counter-rotating spanwise vorticity. Each region of intense vorticity is constituted by smaller regions of co-rotating spanwise vorticity, which appear to merge constructively, to form the large-scale vortical region. Overall, the arrangement resembles a reverse Kármán vortex street with the peak spanwise vorticity $0.1\dot{\theta}_0$.

Each region of lumped vorticity is constituted of two smaller regions of vorticity of similar sign and intensity. This can be seen more clearly in figure 19(*c*), where the regions have been marked by A_1, A_2, B_1 and B_2. From the measurements, the magnitude of the free-stream velocity component is equivalent to the magnitude of the y velocity component. Regions of intense vorticity correspond to regions of distinctive rotational flow in figure 19. In general, the close proximity of regions of high oppositely directed flow in the (x, y)-plane suggests the presence of large velocity gradients. This is indicative of significant out-of-plane motion. Initially, close to the aerofoil, the regions A_1, A_2, B_1 and B_2 start out as linked ring-like structures, but appear to separate into distinct regions as they convect approximately $2c$ further downstream.

Based on the flow visualizations by von Ellenrieder *et al.* (2003), for the same test conditions, a sequence of vortices according to (5.3) are shed in one oscillation cycle.

$$T_1 \rightarrow L_1 \rightarrow T_2 \rightarrow L_2. \tag{5.3}$$

From figure 11 and 19, four smaller structures populate the flow in one cycle. Two pairs of co-rotating flow correspond to the sequence of vortices in (5.3). In figure 11, at phase 1 ($\phi 1$), negative spanwise vorticity, $-\omega_{zc}/\dot{\theta}_0$, appears at the entrance (left) of the measurement area. From the Biot-Savart law, this vorticity would rotate CW. Because the shift in the measurement area relative to the aerofoil, where vorticity
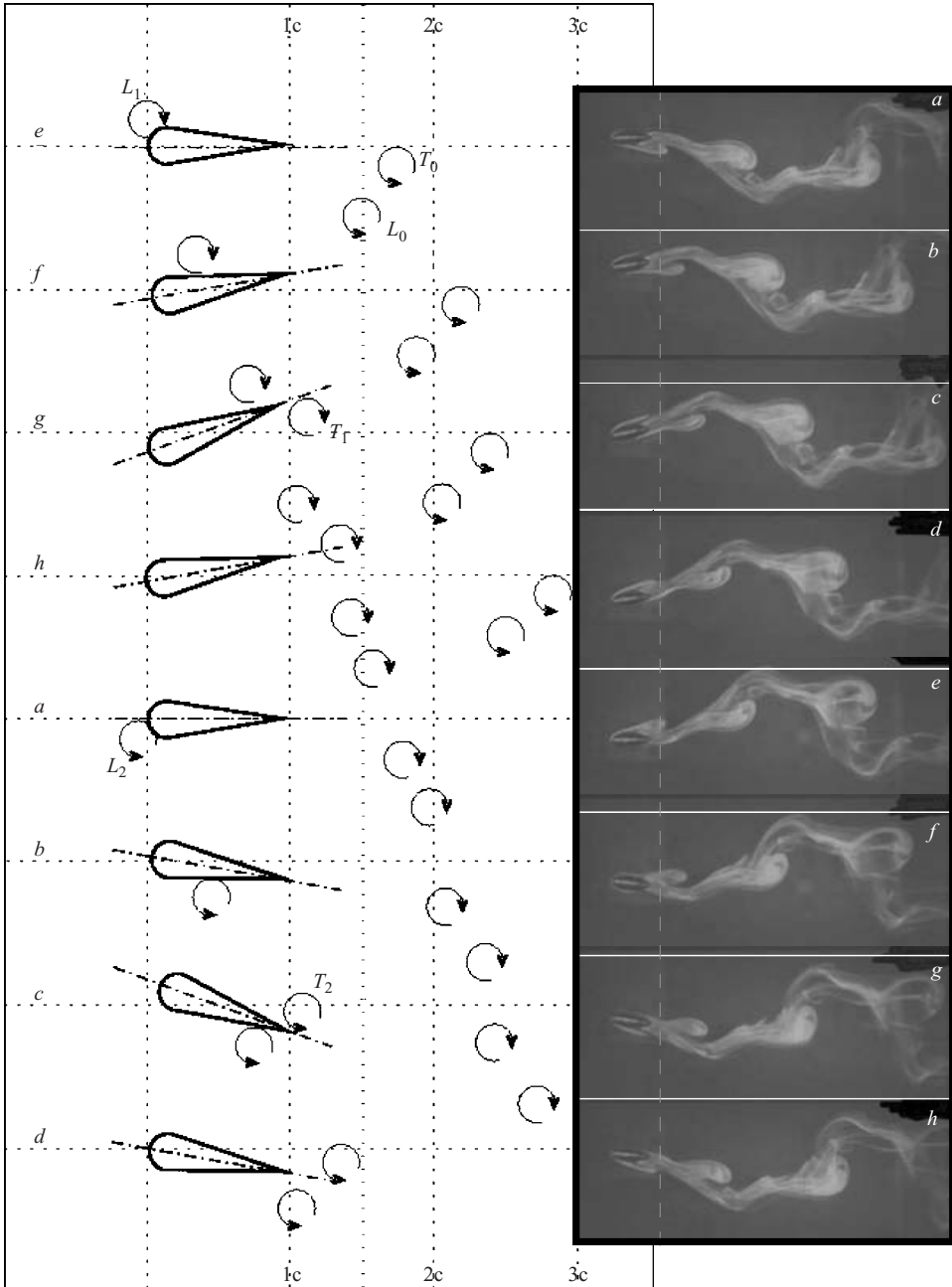
FIGURE 10. Evolution of vorticity behind a three-dimensional flapping wing at $St = 0.35$. The corresponding flow visualizations are shown on the right-hand side. The start of the measurement domain, (region S in figure 7) is demarcated by the dashed vertical line.

would originate, the measured vorticity is mature (created from a previous event). If any vorticity in the flow is assumed to convect approximately at U_∞ and any self-induction is considered small enough to ignore, then the measured negative vorticity originated roughly 1 s earlier.
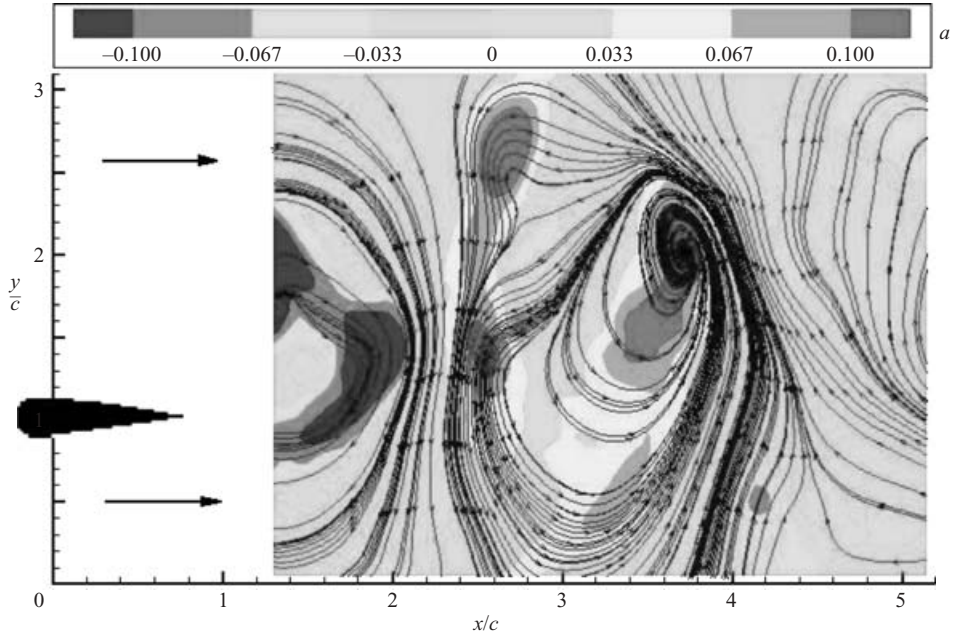
FIGURE 11. Integrated $(\tilde{U}\tilde{V})$ streamline pattern of the periodic mean component of the flow behind a finite flapping wing at $\theta_0 = 5°$; $\psi = 90°$; $St = 0.35$ and phase 1. Iso-contours of the spanwise vorticity, $\omega_z/\dot{\theta}_0$ overlie the streamline pattern.
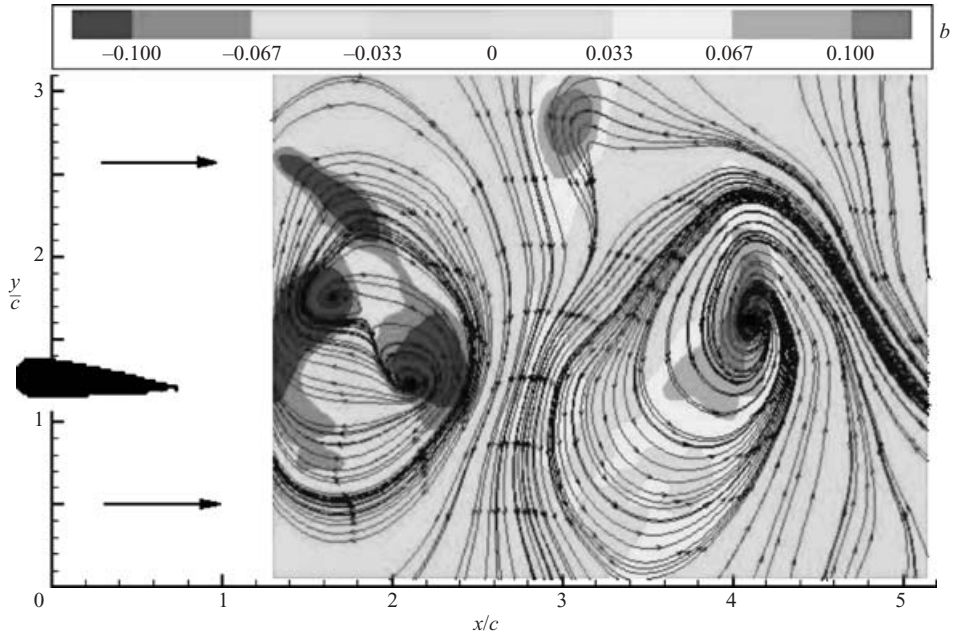
FIGURE 12. As figure 11, but for phase 2.

This corresponds to the $\phi 5$ of the preceding cycle. When the aerofoil reaches $+h_0$, the relative tangential velocity of the flow creates CW rotating flow at $\phi 5$. On the other hand, the aerofoil is expected to experience CCW flow when departing from
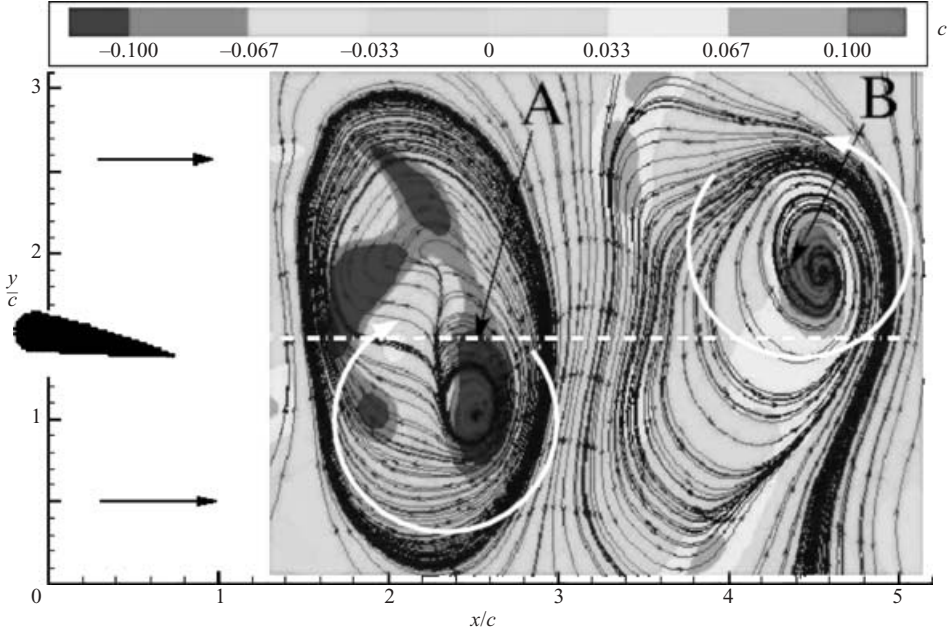
FIGURE 13. As figure 11, but for phase 3.
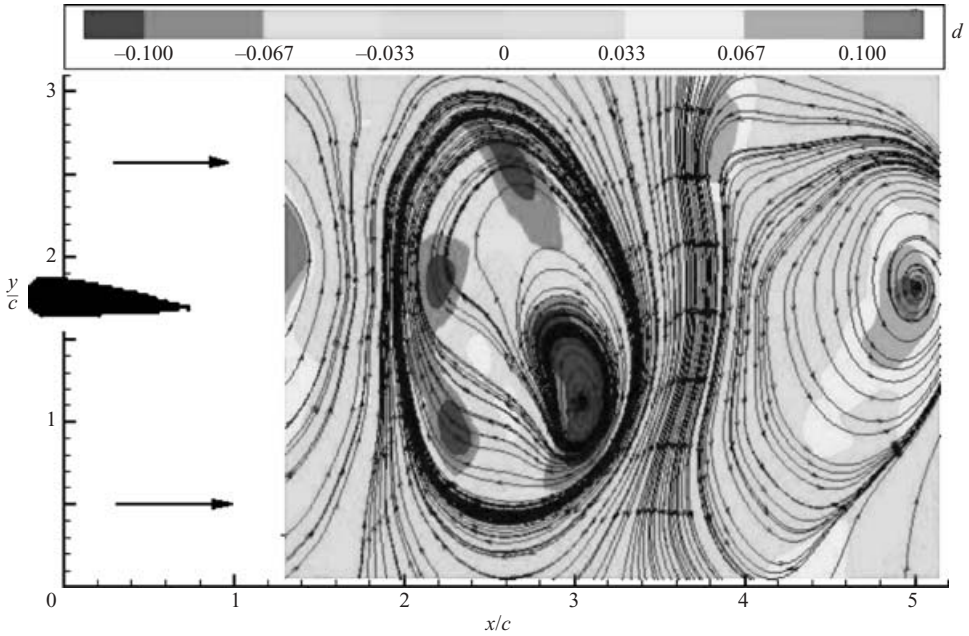
FIGURE 14. As figure 11, but for phase 4.

$-h_0$ at $\phi 1$. Similarly, when the aerofoil reaches the extreme angles of attach at $\phi 3$ and $\phi 7$, the Kutta condition will enforce a separating-flow condition.

The measurements show that two spanwise regions of vorticity, of similar orientation, are shed in each half-cycle. Comparing the measurements to the sequence in (5.3), each half-cycle creates a co-rotating pair of leading- and trailing-edge vortices.
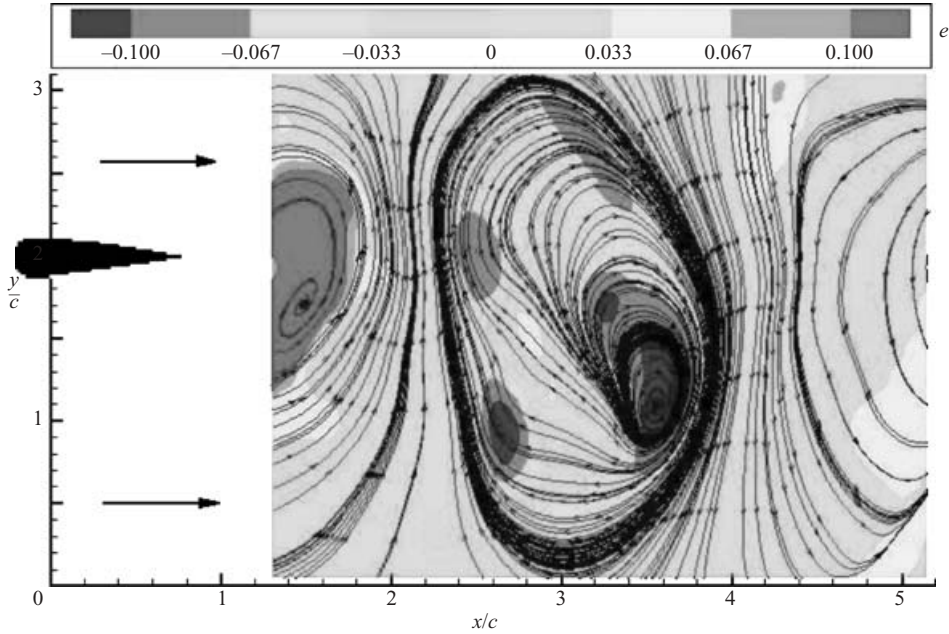
FIGURE 15. As figure 11, but for phase 5.
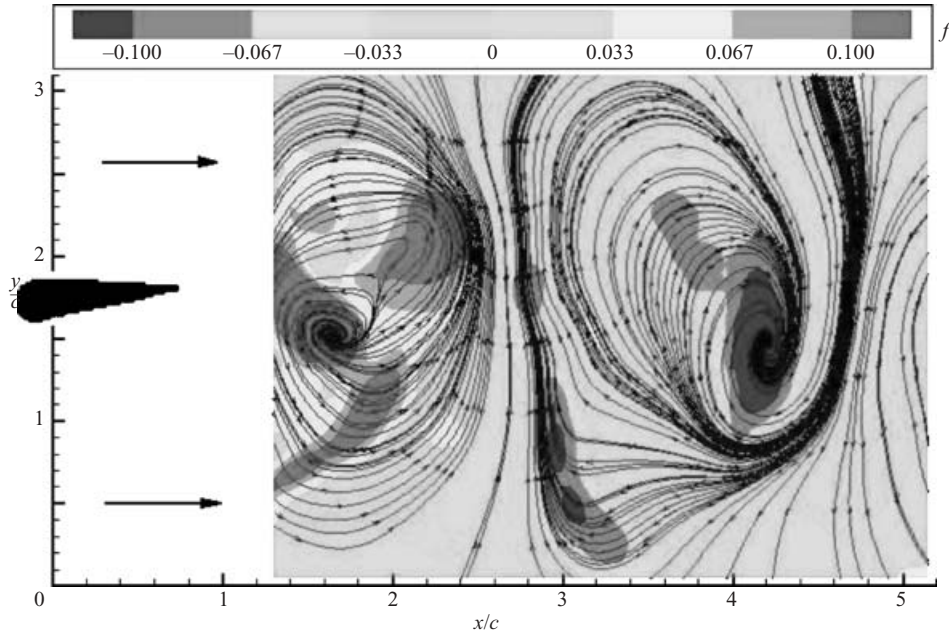
FIGURE 16. As figure 11, but for phase 6.

The maximum heave velocity, $\dot{h}_0 = O(\mathcal{U}_\infty)$. If it is assumed that all vortices formed at the aerofoil convect at the same convection velocity in the x and y directions, simple equations of motion can be used to determine the proximity of shed vorticity relative to the centre of rotation of the aerofoil. This can be calculated for each phase.
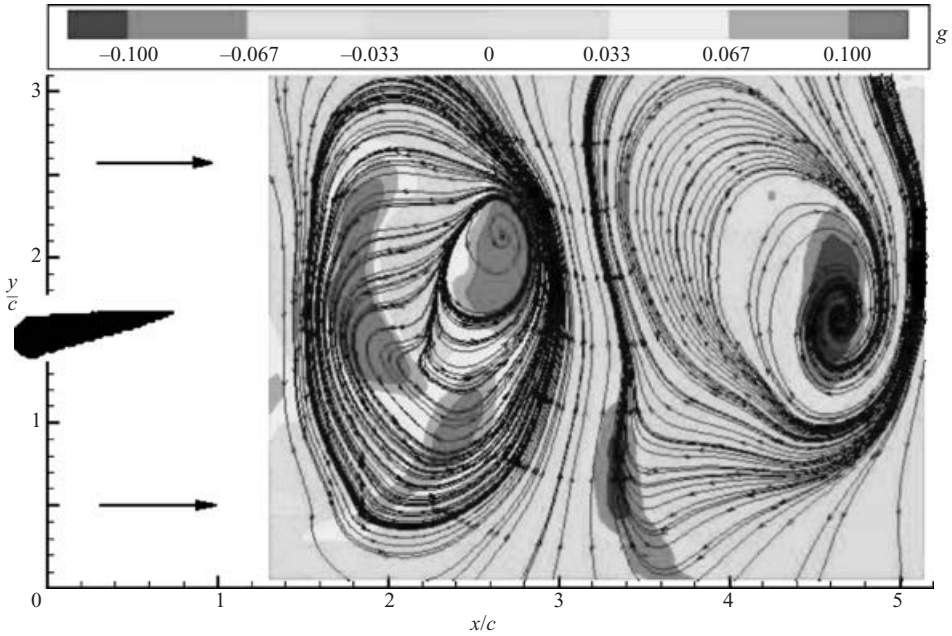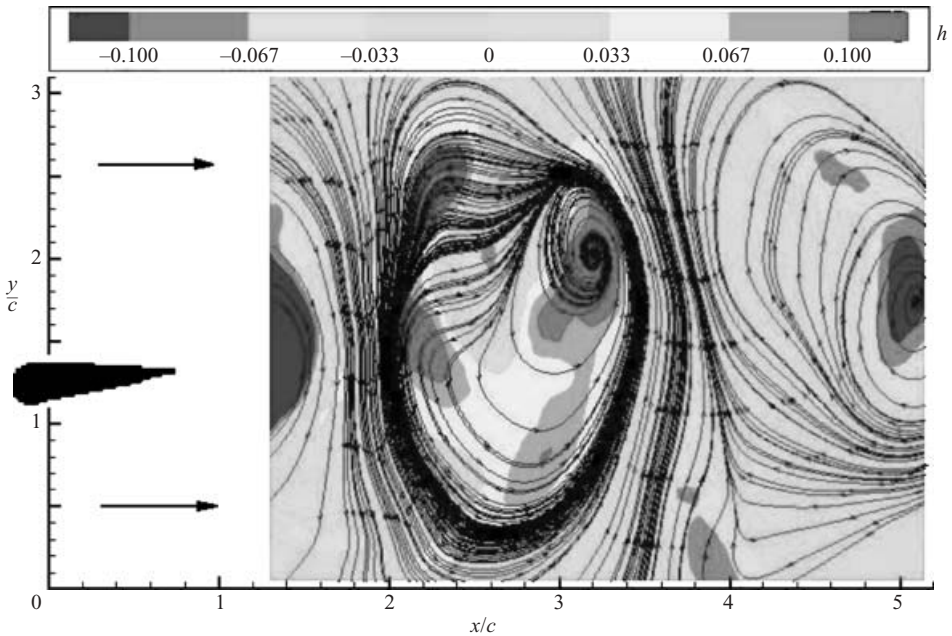
FIGURE 17. As figure 11, but for phase 7.

FIGURE 18. As figure 11, but for phase 8.

Figure 10 is a sketch of the creation, orientation and transport of vortical structures as a result of the tangential velocity of the flow relative to the motion of the aerofoil. This interpretation of the flow is independent of the measurements. It is derived from the kinematics of the aerofoil and expected fluid mechanical behaviour of the flow. This interpretation is inferred from the relative tangential velocity of the flow near the
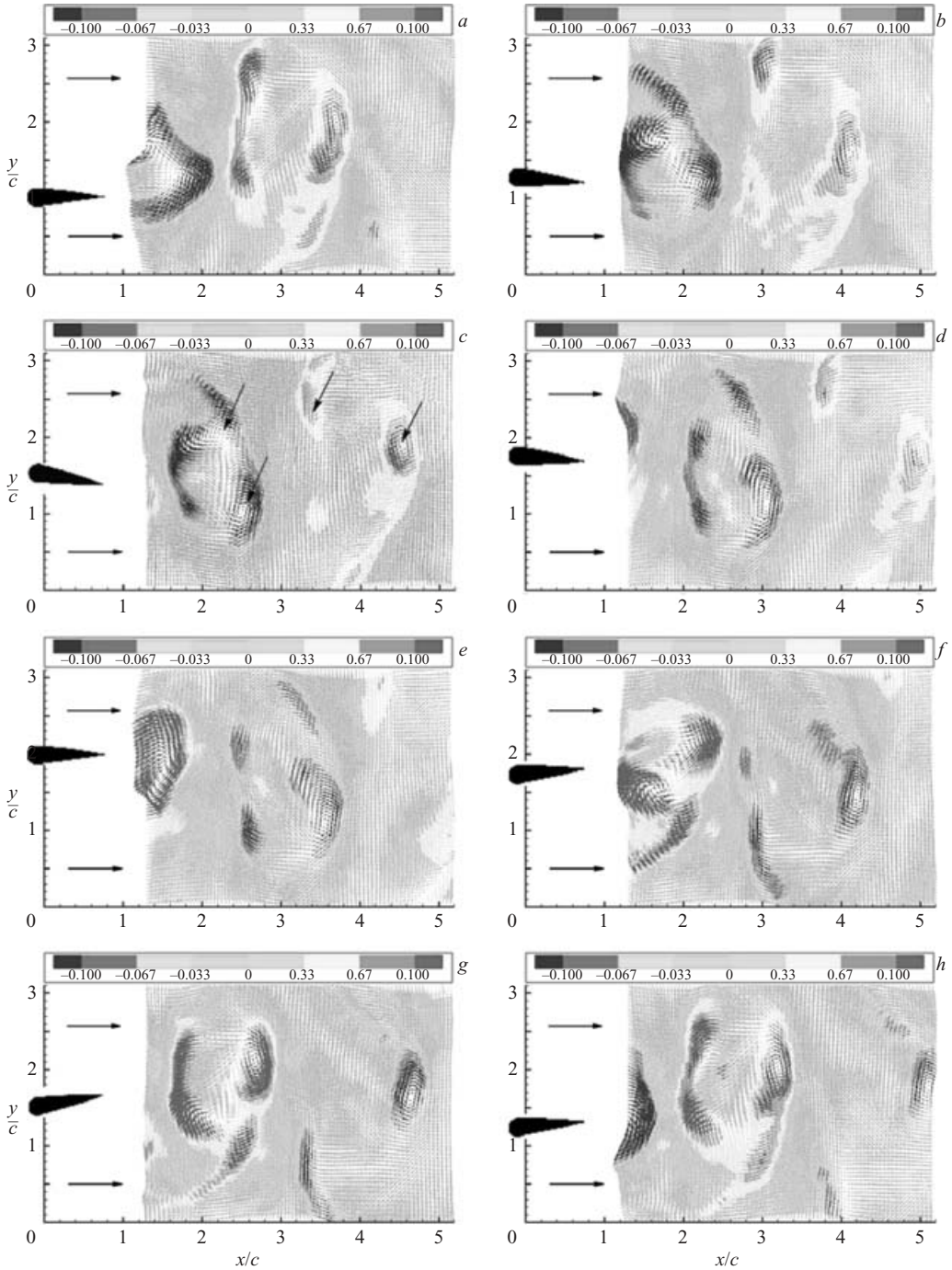
FIGURE 19. In-plane velocity, $(\tilde{U}/U_\infty, \tilde{V}/U_\infty)$ vector field of the periodic mean component of the flow behind a finite flapping wing at $\theta_0 = 5°$; $\psi = 90°$; $St = 0.35$. The vectors are shaded by spanwise vorticity, $\omega_z/\dot{\theta}_0$.

leading- or trailing-edge and the aerofoil motion. The proposed vortex street sketch provides qualitative information of the spatial scale and direction of vorticity. Some consideration of convection of the vortices due to self induction and the mean

flow, is provided. The birth of vorticity at the leading- and trailing-edges are labelled L and T, respectively. The sequence of letters on the left-hand side, corresponds to the phase locations described in table 3. The dashed vertical line at $1.5c$ from the aerofoil trailing edge marks the boundary and the start of the PIV measurement domain.

Figure 10 shows that the flow is expected to be populated by pairs of co-rotating vortices that shed in the sequence described by (5.3). This corresponds also to the sequence observed in the flow visualizations. From the relative x and y tangential velocities, the direction of roll-up of vorticity at the leading-edge, can be inferred. This is shown in figure $10(a, e)$. When the aerofoil is orientated at the extreme pitch angles, $-\theta_0$ and $+\theta_0$, in figures $10(c)$ and $10(g)$ respectively, the Kutta condition imposes a flow-separation condition at the trailing edge, resulting in the formation of T-vortices. The sequence of events that result in the flow pattern depicted in figure 10, is similar to the two-dimensional PIV results of Anderson (1996). The evolution of vorticity depicted in figure 10 is similar to results by others, such as Guglielmini & Blondeaux (2004) and Triantafyllou *et al.* (2004) at similar experimental conditions. In the case of Guglielmini & Blondeaux (2004), the numerical simulation is based on a two-dimensional aerofoil only. In this case, Guglielmini & Blondeaux (2004) comment that the L-vortex is a strong dynamic stall vortex which wraps around a weaker T-vortex of similar sign for the case of $2A/c \geqslant 1$, thus, setting up a Kármán vortex street in the mean flow with the second vortex pair of opposite sign.

5.4. *Reynolds stresses*

Figures 23 to 25 show the phase-averaged components of the Reynolds stresses for the aerofoil. In figure $20(c)$, the focal region of each coherent structure formed by the streamlines, is dominated by very strong positive longitudinal stresses in excess of $0.03U_\infty{}^2$. Each region of high longitudinal stress is constituted by a smaller pair that corresponds to the centroids of regions of rotational flow in figure 19. These regions correspond to areas of both CW and CCW intense vorticity, at all phases, in figure 19.

The periodic mean stress components are shown in figures 20 to 22. In general, at all phases, compared to the periodic mean components, the phase-averaged components of the longitudinal Reynolds stress are greater in magnitude. Since the phase-averaged component includes also the contribution from the mean flow, according to (5.2), this suggests that the mean flow acts to reduce or dampen the mean longitudinal stress levels in the flow field. The maximum phase-averaged stresses $\langle u^2 \rangle \sim 7\tilde{u}^2$. In both cases, the stress field is phase correlated.

In general, both phase-averaged and periodic mean longitudinal stresses exhibit the same spatial distributions, and exhibit similar morphological characteristics between each aerofoil phase. By overlapping $\tilde{u}^2$ with $\langle \tilde{U} \tilde{V} \rangle$ streamlines, regions of high longitudinal stress can be seen overlapping the foci of coherent structures in the flow.

In the case of the periodic mean component of the transverse Reynolds stress in figure 21, there is much less spatial variation from one phase to the next. A region of high $\tilde{v}^2$ remains in a fixed location close to the trailing-edge of the aerofoil. On the other hand, the phase-averaged transverse Reynolds stress distributions in figure 24 appear phase correlated but at peak values four times smaller than the corresponding periodic mean values. When compared to the longitudinal stresses, both periodic and phase-averaged components show that the dominant mechanism in the flow is the transverse Reynolds stress. The transverse direction, y, corresponds to the direction of the heave oscillations of the aerofoil.
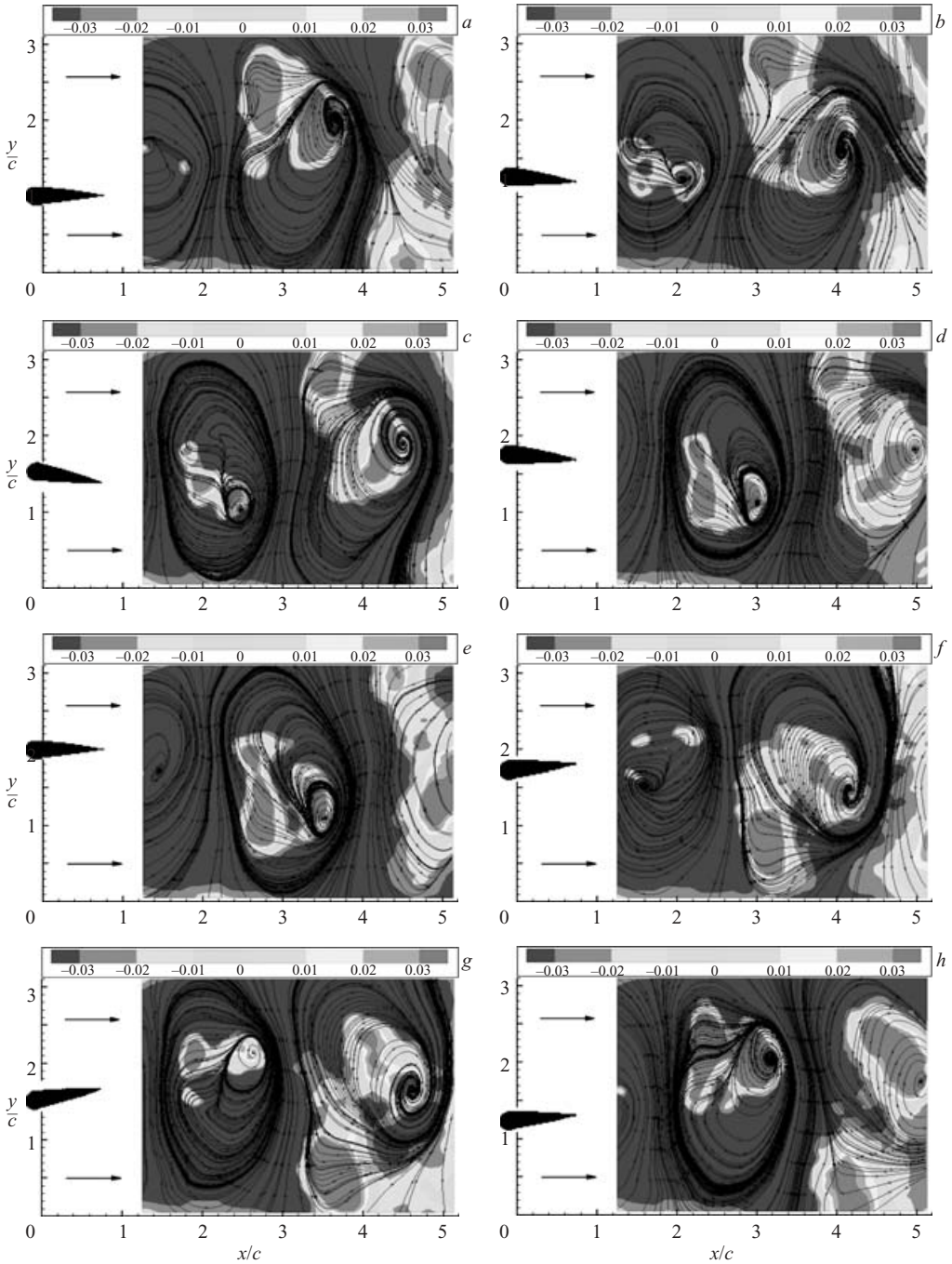
FIGURE 20. Iso-contours of longitudinal Reynolds stress $-(\tilde{u}^2/U_\infty^2)$ overlay with $(\tilde{U}\tilde{V})$ streamline pattern of the flow behind a finite flapping wing at $\theta_0 = 5°$; $\psi = 90°$; $St = 0.35$.

In the case of the shear stress component in figures 25 and 22, the magnitude of the peak phase-averaged component equals the magnitude of the peak periodic mean component. The peak shear stress for both components is roughly $0.4U_\infty^2$. The spatial distribution and temporal variation for the phase-averaged and periodic mean
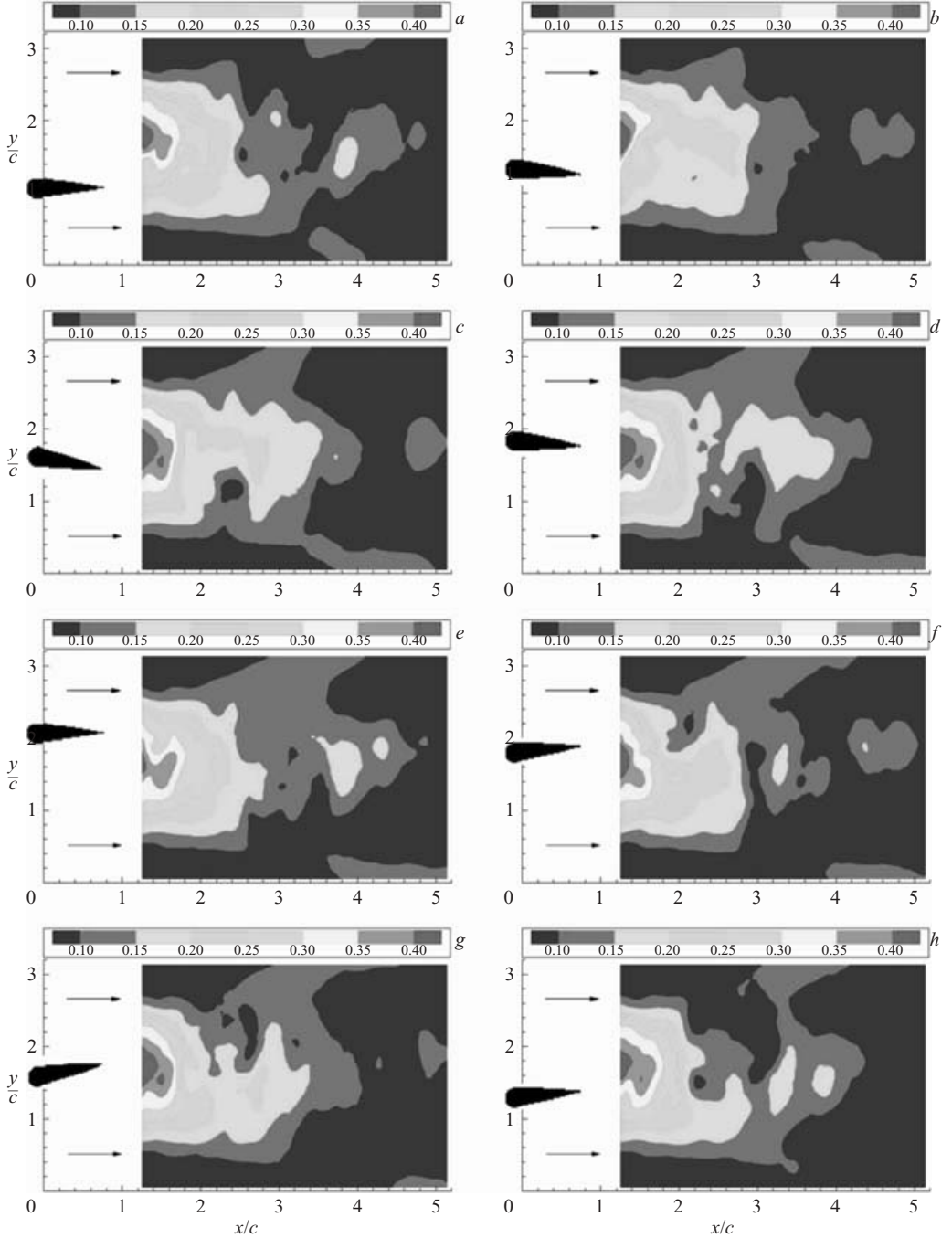
FIGURE 21. Iso-contours of transverse Reynolds stress $-(\tilde{v}^2/U_\infty^2)$ of the flow behind a finite flapping wing at $\theta_0 = 5°$; $\psi = 90°$; $St = 0.35$.

components exhibit the same morphological characteristics. Thus, in the case of the shear stress components, the mean flow has little influence. When the shear stress contours in figure 22 are superimposed onto $\langle \tilde{U}\tilde{V} \rangle$ streamlines, possible correlation between coherent structures in the flow and high measured shear stress, can be
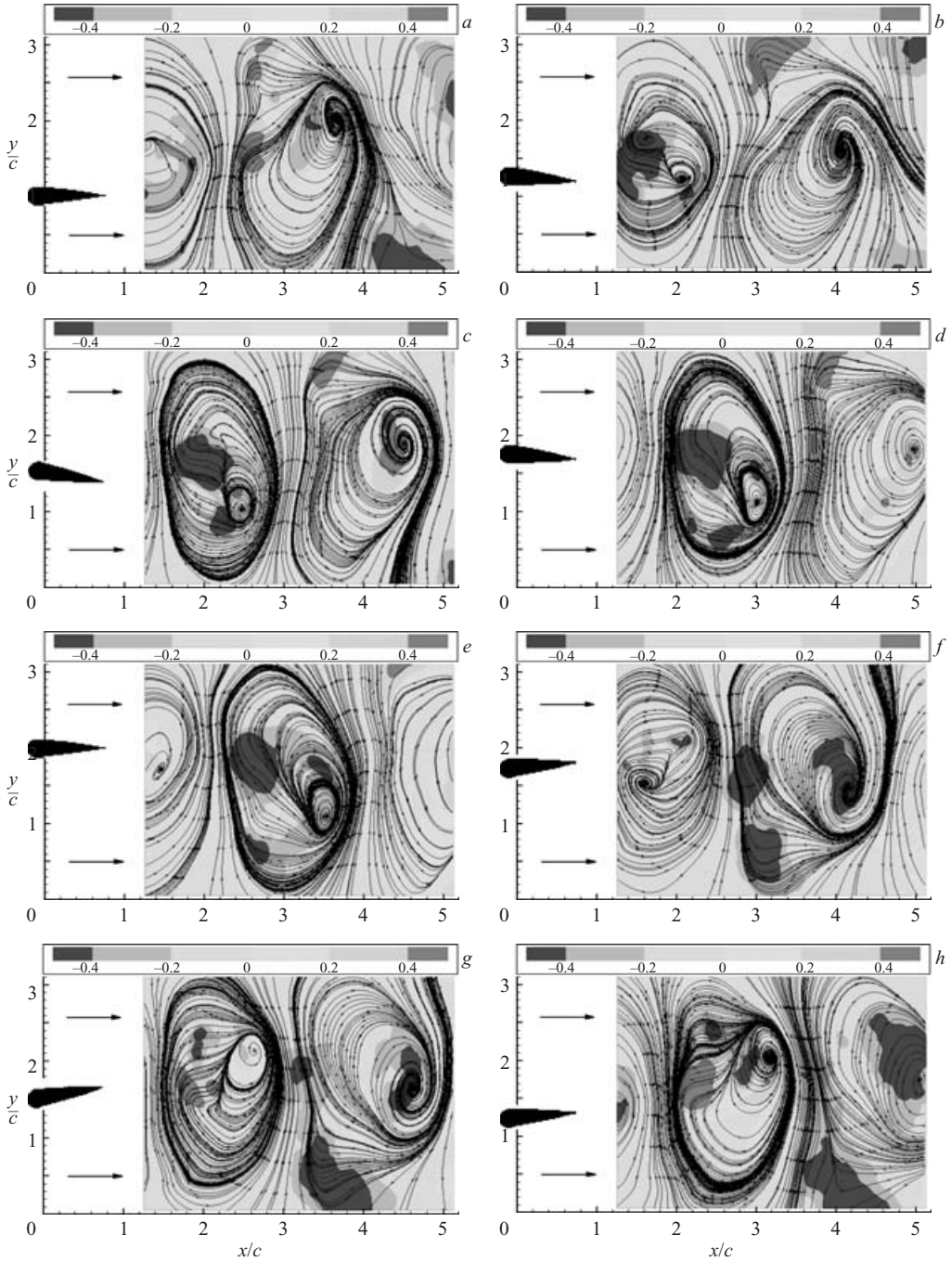
FIGURE 22. Iso-contours of the in-plane shear Reynolds stress $-(\tilde{u}\tilde{v}/U_\infty^2)$ overlay with $\langle \tilde{U}\tilde{V}\rangle$ integrated streamline pattern of the flow behind a finite flapping wing at $\theta_0 = 5°$; $\psi = 90°$; $St = 0.35$.

identified. Figure 22 suggests that there is no clear correlation between coherent foci or in-plane Reynolds shear stress. The shear stress is greater than the peak normal stresses, based on the phase-averaged measurement, by a factor of 2. In the case of the
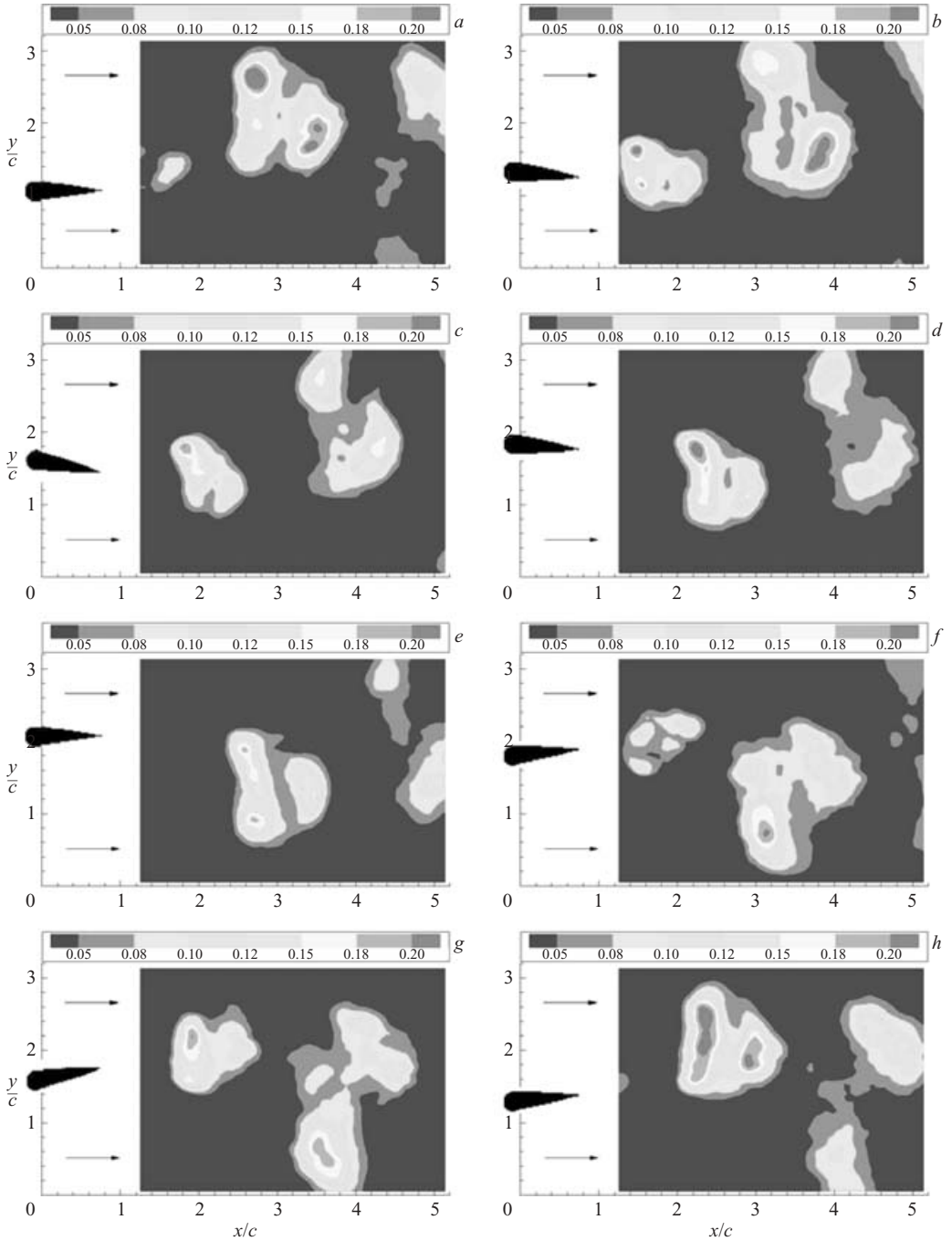
FIGURE 23. Iso-contours of the phase-averaged longitudinal Reynolds stress $-(\langle u^2 \rangle / U_\infty^2)$ of the flow behind a finite flapping wing at $\theta_0 = 5°$; $\psi = 90°$; $St = 0.35$.

periodic mean measurement, the peak shear stress is as large as the peak transverse stress component.

Overall, the stress fields show the existence of separate lumped regions corresponding to the four separate regions of vorticity in one oscillation cycle. The
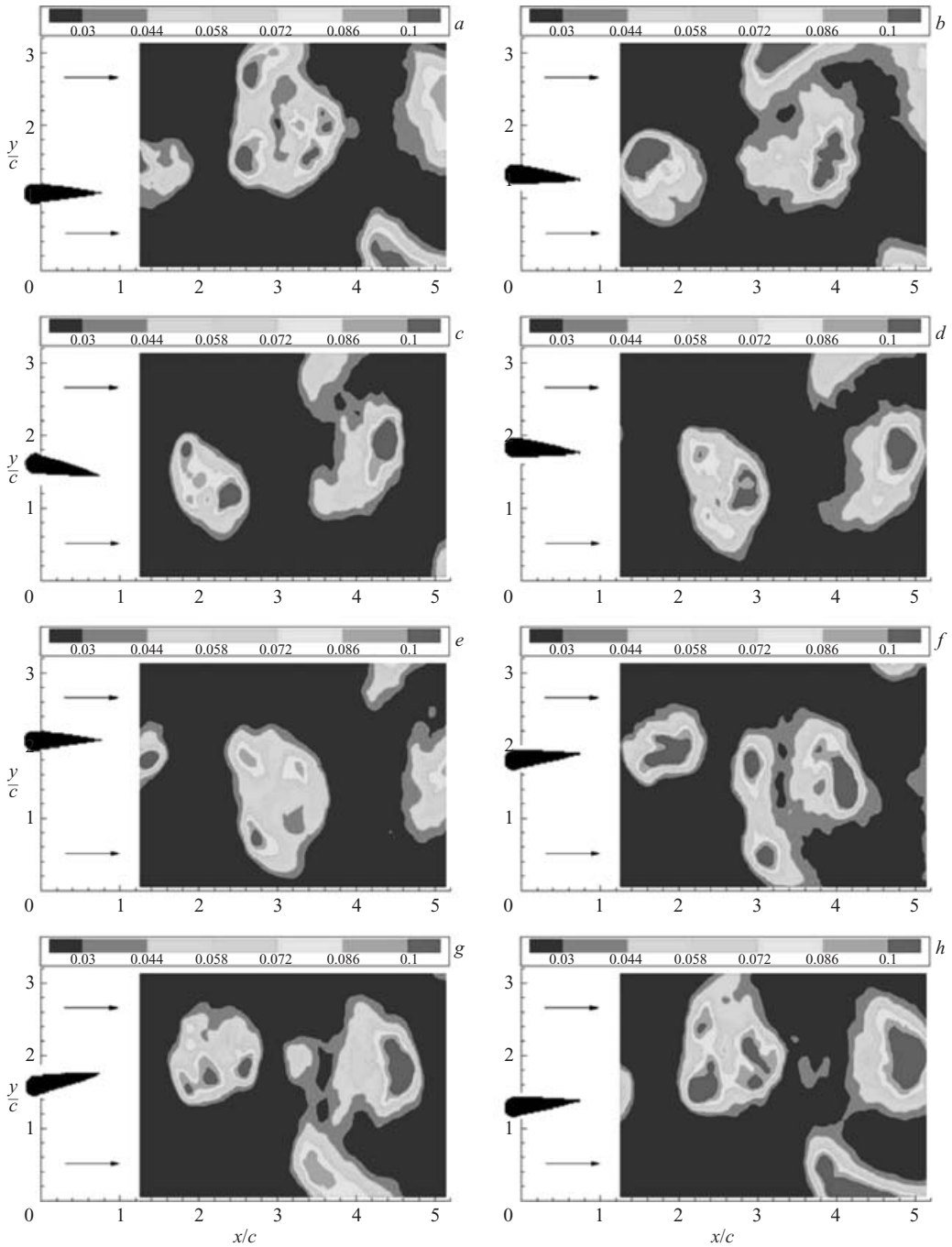
FIGURE 24. Iso-contours of the phase-averaged transverse Reynolds stress $- (\langle v^2 \rangle / U_\infty^2)$ of the flow behind a finite flapping wing at $\theta_0 = 5°$; $\psi = 90°$; $St = 0.35$.

spanwise vortex pairing that is observed in the initial stages of development of the flow corresponds to regions of high Reynolds stresses. The data show that the phase-averaged flow is dominated by the periodic mean component of the organized wave and that the mean flow has little influence on Reynolds stresses in the flow. The
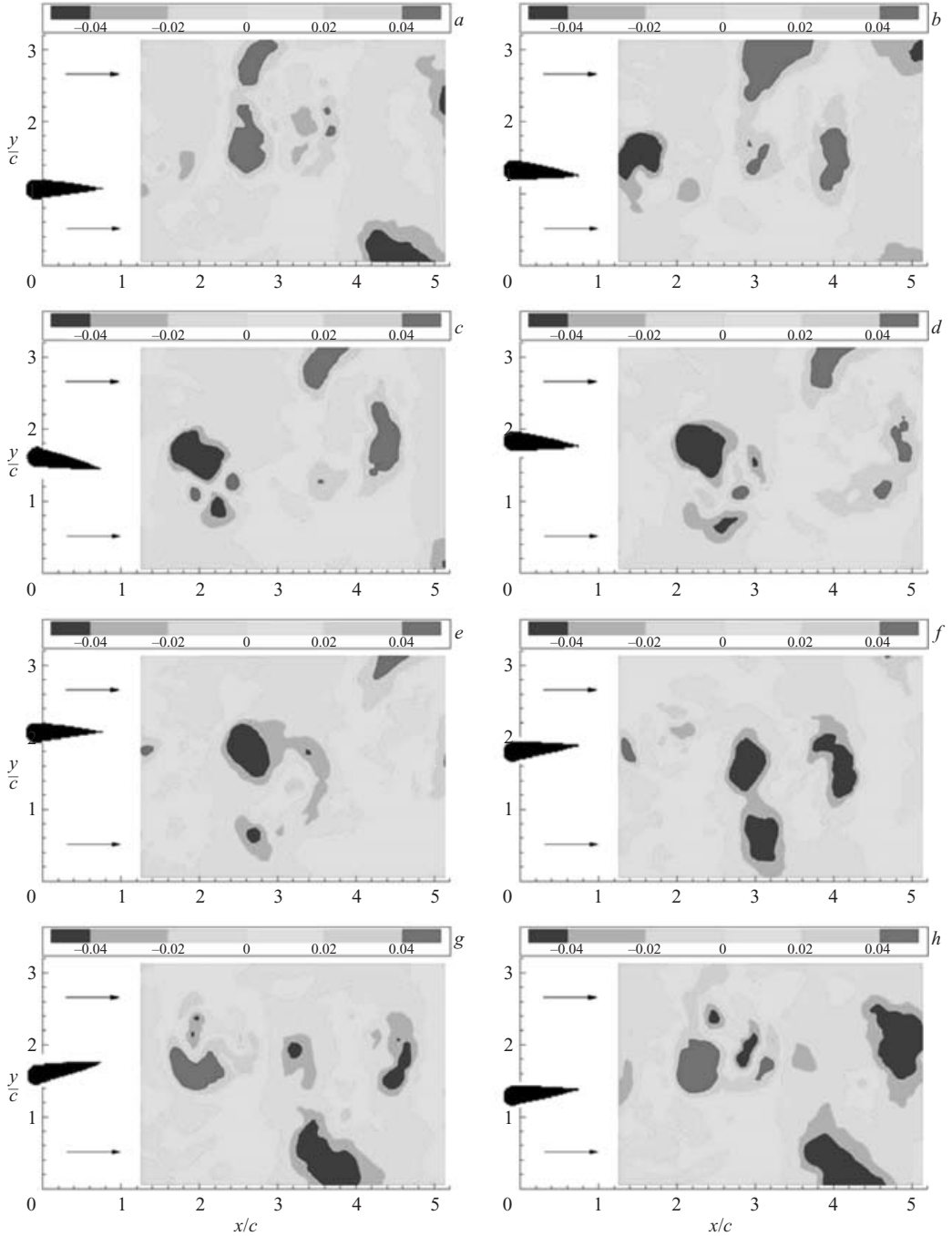
FIGURE 25. Iso-contours of the phase-averaged shear Reynolds stress $-(\langle uv \rangle / U_\infty^2)$ of the flow behind a finite flapping wing at $\theta_0 = 5°$; $\psi = 90°$; $St = 0.35$.

apparent dominance of the anisotropic component of the two-dimensional Reynolds stress tensor suggests that this is a major mechanism for dissipation of turbulent kinetic energy from the aerofoil motion.

6. Concluding remarks

The flow visualization images show pairs of alternating leading- and trailing-edge vortices. The measurements show that each vortex pair is co-rotating. This results in constructive merging of leading- and trailing-edge vortices to form stronger large-scale regions of spanwise vorticity.

The numerical findings in Blondeaux *et al.* (2005*a*) show differences in detail between the wake model inferred from the flow visualizations of von Ellenrieder *et al.* (2003) and their isosurface vortex tubes. The gross appearances of the wakes are qualitatively similar. As mentioned by Blondeaux *et al.* (2005*a*), the use of isosurface criteria in trying to establish the wake structure has the limitation that it cannot avoid losing the details of the vortex structures in those regions where vorticity is large. Thus, while several isosurface criteria were tried by Blondeaux *et al.* (2005*a*) (vorticity, pressure minima and the complex eigenvalues of the velocity gradient tensor), not all parts of the vortex structure could be visualized. This is especially apparent in regions of strong vortex interaction and reconnection. Dong *et al.* (2005) presented the results of a numerical study of an oscillating wing. In comparison with the wing used in von Ellenrieder *et al.* (2003) and Blondeaux *et al.* (2005*a*), the aerofoil cross-section used by Dong *et al.* (2005) was much thinner (12 % thickness), was operated at almost twice the Strouhal number and had a rounded trailing edge. Thus, the findings of Dong *et al.* (2005) can be expected to differ somewhat. Dong *et al.* (2005) reported that the occurrence of two chains of vortical structures in the wake is strongly dependent upon the aspect ratio of the wing. For a Strouhal number of 0.6 and lower, and wing aspect ratios of 1.27 and 2.55, a wake characterized by two chains of vortical structures is reported. However, for aspect ratios of 5.09 and ∞ (two-dimensional), a single wake structure is observed. As remarked in later sections of the Dong *et al.* (2005) paper, the structure of the wake is qualitatively similar to that observed in the experiments of von Ellenrieder *et al.* (2003).

The spatio-temporal variation of vorticity in the flow field show that the shedding process is phase locked with the forced motion of the aerofoil. The flow field is populated by structures of various length scales, in the plane of symmetry. The evolution of these structures, as well as the interaction of structures in the flow field, is indicative of the complex three-dimensional nature of this flow. The flow is characterized by a pair of coherent structures of positive and negative vorticity which shed in each oscillation cycle. To characterize the morphological aspects of the flow adequately, more velocity and spatial information is required.

The dominant mechanism for the transfer of momentum from the flapping aerofoil, based on the midspan measurements, appears to be the transverse Reynolds stress component. This acts in the direction of flapping. The apparent dominance of the wave component of the forced flapping motion, in the Reynolds stresses, indicate qualitatively, that the large-scale disturbances introduced by the sinusoidal motions are primarily responsible for thrust production and the flow character. Aerofoil kinematics drive, primarily, the morphological characteristics of the flow.

REFERENCES

ANDERSON, J. M. 1996 Vortex control for efficient propulsion. PhD thesis, Massachusetts Institute of Technology and Woods Hole Oceanographic Institute.

ANDERSON, J. M., STREITLIEN, K., BARRETT, D. S. & TRIANTAFYLLOU, M. S. 1998 Oscillating foils of high propulsive efficiency. *J. Fluid Mech.* **360**, 41–72.

BETZ, A. 1912 Ein beirtrag zur erklarung des segelfluges. *Z. Flugtech. Motorluftschiff.* **3**, 269–272.

BISHOP, R. E. D. & HASSAN, A. Y. 1963 The lift and drag forces on a circular cylinder oscillating in a flowing fluid. *Proc. R. Soc. Lond.* A **277**, 51–75.

BLONDEAUX, P., FORNARELLI, F., GUGLIELMINI, L., TRIANTAFYLLOU, M. S. & VERZICCO, R. 2005a Numerical experiments on flapping foils mimicking fish-like locomotion. *Phys. Fluids* **17**, 113601.

BUCHHOLZ, J. H. J. & SMITS, A. J. 2005 On the evolution of the wake structure produced by a low-aspect-ratio pitching panel. *J. Fluid Mech.* **546**, 433–443.

CANTWELL, B. & COLES, D. 1983 An experimental study of entrainment and transport in the turbulent near wake of a circular cyclinder. *J. Fluid Mech.* **136**, 321–351.

CHENG, H. K. & MURILLO, L. E. 1984 Lunate-tail swimming propulsion of curved lifting line in unsteady flow. Part 1. Asymptotic theory. *J. Fluid Mech.* **143**, 327–350.

CHONG, M., PERRY, A. & CANTWELL, B. 1990 A general classification of three-dimensional flow fields. *Phys. Fluids* **2** (5), 765–777.

DELAURIER, J. D. & HARRIS, J. M. 1982 Experimental study of oscillating-wing propulsion. *J. Aircraft* **19**, 368–373.

DONG, H., MITTAL, R., BOZKURRTAS, M. & NAJJAR, F. 2005 Wake structure and performance of finite aspect-ratio flapping foils. *AIAA Paper* 2005–81.

DRUCKER, E. G. & LAUDER, G. V. 1999 Locomotor forces on a swimming fish: three-dimensional vortex wake dynamics quantified using digital particle image velocimetry. *J. Exp. Bioll.* **202**, 2393–2412.

VON ELLENRIEDER, K. D., PARKER, K. & SORIA, J. 2003 Flow structures behind a heaving and pitching finite-span wing. *J. Fluid Mech.* **490**, 129–138.

FOURAS, A. & SORIA, J. 1998 Accuracy of out-of-plane vorticity measurements using in-plane velocity vector field data. *Exps. Fluids* **25**, 409–430.

FREYMUTH, P. 1988 Propulsive vortical signature of plunging and pitching airfoils. *AIAA J.* **26**, 880–883.

GARRICK, I. E. 1936 Propulsion of a flapping and oscillaing aerofoil. *NACA Tech. Rep.* 567.

GUGLIELMINI, L. & BLONDEAUX, P. 2004 Propulsive efficiency of oscillating foils. *Eur. J. Mech. B/Fluids* **23**, 255–278.

HAMA, F. R. 1962 Streaklines in a perturbed shear flow. *Phys. Fluids* **5** (6), 644–650.

HOVER, F. S., HAUGSDAL, O. & TRIANTAFYLLOU, M. S. 2003 Control of angle of attack profiles in flapping foil propulsion. *J. Fluids Struct.* **19**, 37–47.

HUSSAIN, A. K. M. F. 1986 Coherent structures and turbulence. *J. Fluid Mech.* **173**, 303–356.

HUSSAIN, A. K. M. F. & REYNOLDS, W. C. 1970 The mechanics of an organized wave in turbulent shear flow. *J. Fluid Mech.* **41**, 241–258.

JONES, K. D., DOHRING, C. M. & PLATZER, M. F. 1996 Wake structures behind plunging airfoils: a comparison of numerical and experimental results. *AIAA Paper* 96-0078.

JONES, K. D., CASTRO, B. M., MAHMOUD, O., POLLARD, S. J., PLATZER, M. F., NEEF, M. F., GONET, K. & HUMMEL, D. 2002 A collaborative numerical and experimental investigation of flapping-wing propulsion in ground effect. *AIAA Paper* 2002-0706.

KATZ, J. & WEIHZ, D. 1978 Behaviour of vortex wakes from oscillating airfoils. *J. Aircraft* **50**, 861–863.

KATZMAYR, R. 1922 Effect of periodic changes in the angle of attack on behavior of airfoils. *NACA Tech. Rep.* 147.

KNOLLER, R. 1909 Die gesetze des luftwiderstandes. *Flug Motortechnik* **3**(21), 1–7.

KOOCHESFAHANI, M. M. 1989 Vortical patterns in the wake of an oscillating airfoil. *AIAA J.* **27**, 1200–1205.

LOZANO, A., KOSTAS, J. & SORIA, J. 1998 Use of holography in particle image velocimetry measurements of a swirling flow. *Exps. Fluids* **26**, 111–128.

PARKER, K., VON ELLENRIEDER, K. & SORIA, J. 2002*a* The effects of phase angle on the vortical signatures behind a flapping airfoil of finite aspect ratio. In *Proc. 10th Intl Symp. Flow Visualization* (ed. Takahashi & K. Ohmi). Japanese Visualization Society.

PARKER, K., VON ELLENRIEDER, K. & SORIA, J. 2002*b* Flow visualization of the effect of pitch amplitude changes on the vortical signatures behind a three dimensional flapping airfoil. In *Proc. SPIE, vol. 5058, Optical Technology and Image Processing for Fluids and Solids Diagnostics* (ed. G. X. Shen, S. S. Cha, F.-P. Chiang & C. R. Mercer), pp. 331–343.

PARKER, K., VON ELLENRIEDER, K. & SORIA, J. 2003 Strouhal number dependence of the vortex aspect ratio behind a three dimensional heaving airfoil. In *Proc. 2nd Intl Conf. on Heat Transfer, Fluid Mechanics and Thermodynamics, Zambia. HEFAT* (ed. J. Meyer), Paper A121. The University of Petoria.

PARKER, K., VON ELLENRIEDER, K. & SORIA, J. 2004 Stereoscopic PIV measurements of the flow past a circular cylinder at Reynolds number 15 000, In *Proc. 15th Australasian Fluid Mech. Conf.* (ed. M. Behnia, W. Lin & G. D. McBain), Paper AFMC00226, University of Sydney, (CD-ROM).

PARKER, K., VON ELLENRIEDER, K. & SORIA, J. 2005 Using stereo multigrid DPIV measurements to investigate the vortical skeleton behind a finite-span flapping wing. *Exps. Fluids* **39**, 281–298.

PLATZER, M. F. 2001 Flapping wing propulsion. *Tech. Rep.* Naval Postgraduate School-Monterey, CA.

POPE, S. B. 2000 *Turbulent Flows*. Cambridge University Press.

REYNOLDS, W. C. & HUSSAIN, A. K. 1972 The mechanics of an organized wave in turbulent shear flow. Part 1. Theoretical models and comparisons with experiments. *J. Fluid Mech.* **54**, 263–290.

SORIA, J. 1996 An investigation of the near wake of a circular cylinder using a video-based digital cross-correlation particle image velocimetry technique. *Expl Thermal Fluid Sci.* **12**, 221–233.

SORIA, J. 1998 Multigrid approach to cross-correlation digital PIV and HPIV analysis. In *Proc. 13th Australasian Fluid Mech. Conf.* (ed. J. Soria), Paper AFMC0010. Monash University (CD-ROM).

TENNEKES, H. & LUMLEY, J. 1972 *A First Course in Turbulence*. MIT Press.

TRIANTAFYLLOU, M. S., TRIANTAFYLLOU, G. S. & YUE, D. K. P. 2000 Hydrodynamics of fishlike swimming. *Annu. Rev. Fluid Mech.* **32**, 33–53.

TRIANTAFYLLOU, M. S., TECHERT, A. H. & HOVER, F. S. 2004 Review of experimental work in biomimetics foils. *J. Ocean Engng* **29**, 585–594.

TUNCER, I. A., WALZ, R. & PLATZER, M. F. 1998 A computational study of the dynamic stall of a flapping airfoil. *Tech. Rep.* 98-2519. Naval Postgraduate School, Monterey, CA.